# Rayleigh and depinning instabilities of forced liquid ridges on heterogeneous substrates

Philippe Beltrame[*]
*UMR EmmaH 1114, Département de Physique, Université d'Avignon, F-84000 Avignon, France*

Edgar Knobloch[†]
*Department of Physics, University of California, Berkeley, California 94720, USA*

Peter Hänggi[‡]
*Institut für Physik, Universität Augsburg, D-86135 Augsburg, Germany*

Uwe Thiele[§]
*Department of Mathematical Sciences, Loughborough University, Loughborough, Leicestershire, LE11 3TU, United Kingdom*

(Received 23 July 2010; published 18 January 2011)

Depinning of two-dimensional liquid ridges and three-dimensional drops on an inclined substrate is studied within the lubrication approximation. The structures are pinned to wetting heterogeneities arising from variations of the strength of the short-range contribution to the disjoining pressure. The case of a periodic array of hydrophobic stripes transverse to the slope is studied in detail using a combination of direct numerical simulation and branch-following techniques. Under appropriate conditions the ridges may either depin and slide downslope as the slope is increased, or first break up into drops via a transverse instability, prior to depinning. The different transition scenarios are examined together with the stability properties of the different possible states of the system.

DOI: 10.1103/PhysRevE.83.016305 PACS number(s): 47.20.Ky, 47.55.nb, 68.08.−p, 68.15.+e

## I. INTRODUCTION

Experiments on sliding drops on solid substrates or on moving contact lines show that the driving force must exceed a nonzero threshold in order that motion results [1–4]. These observations are at variance with the theoretical predictions obtained for ideally smooth and homogeneous substrates for which motion starts for arbitrarily small driving force [2,5–9]. This discrepancy between experiment and theory is believed to be caused by chemical heterogeneities and/or topographic roughness that are always present on real substrates [10–14]. A finite force is then needed to depin the contact line or entire drop from the heterogeneity [3,12,13,15–18].

More generally, micro- or mesoscale heterogeneities are expected to affect the macroscopic movement of drops. For instance, they are responsible for contact angle hysteresis [1,2,19], the roughening of contact lines [1,2,20–22], and the stick-slip motion of weakly driven contact lines [17,23]. Heterogeneities may also slow down or stop entirely the long-time coarsening of drop patterns in dewetting [24–26].

These considerations apply to drops or liquid fronts (contact lines) moving down an inclined substrate due to a gradient of potential energy [3,5,27,28]. However, they also apply to motion of drops or fronts caused by a temperature gradient along the substrate (resulting in Marangoni forces due to surface tension gradients) [29,30], or by wettability gradients [8,10,31–34].

One approach to real (i.e., nonidealized) substrates is to consider the limit of random heterogeneities [20–22,35,36]. Another approach focuses on the effect of individual well-defined defects [11,35,37,38]. Recently, the latter approach was extended to study the depinning dynamics of drops on substrates with a periodic array of precisely specified defects [39–41]. The approach employs a thin film evolution equation with a spatially modulated disjoining pressure and enables one to (i) study the depinning transition employing tools from dynamical systems theory and bifurcation theory, and (ii) investigate the dynamics of the stick-slip motion that occurs after depinning on substrates with many defects. Contact line and drop motion on regularly patterned substrates [42–45] is in fact of considerable importance in various microfluidic and nanotechnological applications [46–50]. Single-cell assays, i.e., miniaturized devices for cell biology that consist of chemically and/or physically structured substrates, provide a good example. In this device each cell may be confined in an individual "reaction chamber," e.g., a drop of water on a hydrophilic spot. A pattern of such spots allows for parallel analysis of a large number of cells [51]. Driven drop motion on a regular heterogeneous substrate with a well-defined wettability period is also related to the motion of drops of partially wetting liquid on a horizontal rotating cylinder [52].

At first sight the qualitative behavior of driven drops on substrates with a well-defined array of defects described in previous studies of the problem in a two-dimensional (2D) setting [39,40] agrees well with the results of three-dimensional (3D) computations [41]. In a 2D system pinned drops can depin by two different mechanisms depending on the wettability properties of the defect, the drop size, and the driving force. The drops are either pinned by a hydrophilic defect at their back or by a hydrophobic defect at their front. For the parameters

[*]philippe.beltrame@univ-avignon.fr
[†]knobloch@berkeley.edu
[‡]peter.hanggi@physik.uni-augsburg.de
[§]http://www.uwethiele.de; u.thiele@lboro.ac.uk

 

investigated in Ref. [39] the following depinning scenarios are found. In the hydrophilic case the pinned drop stretches quasistatically as the driving force increases but eventually loses stability through a "sniper" (or saddle-node infinite period) bifurcation, resulting in depinning. For forces larger than this critical force the drop slides in a periodic motion over the periodic array of defects. Theory implies that the mean drop speed beyond depinning should vanish as the square root of the distance from the sniper bifurcation [53] and this behavior is indeed observed in simulations. Each period of the resulting stick-slip motion consists of two distinct evolution phases that take place on distinct time scales: the drop slowly stretches away from the defect but once it breaks away it slides rapidly over to the next defect. The time scales for the "sticking" and "sliding" phases differ greatly close to the bifurcation, and the behavior that results resembles closely the experimentally observed stick-slip motion. The situation is richer for hydrophobic defects that pin the drop by blocking it in front. In this case, in addition to the steady-state sniper bifurcation, depinning can also occur via a Hopf bifurcation, depending on the details of the defect [39].

A recent study of the depinning of 3D drops from hydrophobic and hydrophilic line defects [41] employing continuation and time-stepping algorithms [54] establishes a qualitative similarity between the 2D and 3D cases and supports the widely held expectation that studies of 2D thin film systems provide useful information about more realistic 3D systems. However, significant differences do exist. These are mostly related to the additional degrees of freedom of the 3D system. For instance, the 3D drop can, under appropriate circumstances, employ depinning pathways via morphological changes that are unavailable to a 2D drop. In the case of a hydrophilic defect the backward thread that connects the drop to the defect may gradually thin, whereas in the hydrophobic case the drop may "probe" the barrier locally by sending out an advancing protrusion over the defect [41]. In fact, the 3D system has a number of features that have no counterpart in the 2D system, beyond the details of the depinning behavior of individual drops. The present study is dedicated to their analysis.

Our starting point is the observation that all 2D drop solutions correspond in a 3D setting to spanwise-invariant ridge solutions. It follows therefore that *all* results of [39,40] remain valid in a 3D setting provided one imposes translation symmetry in the spanwise direction. Thus stable ridge and drop solutions of identical liquid volume may coexist. Either of these solution types may become unstable as parameters are varied giving rise to branches of solutions that have not yet been studied. In the limit of zero driving (e.g., a horizontal substrate when gravity is the driving force) and a homogeneous substrate this question is related to the characteristics of the Plateau-Rayleigh instability [55,56] of a static ridge (sometimes called a truncated cylinder) [57,58].

In a driven 3D system on a heterogeneous substrate the question translates into (i) an investigation of the lateral stability of pinned and sliding spanwise-invariant ridges, and (ii) the longitudinal stability of streamwise rivulets whose diameter is modulated by the heterogeneities. In both cases we expect changes of stability that give rise to "new" branches of (i) spanwise modulated ridges and (ii) "wavy rivulets," respectively. These states have no counterpart in the 2D case. We are interested in particular in the relation between the stability of the rivulets [59] and the existence of depinned sliding drop solutions. The combination of these aspects of the problem together with 2D and 3D depinning characteristics obtained previously [39–41] provides a fairly complete picture of the 3D problem and of the relation among static and sliding ridges, static and sliding drops, and steady or wavy rivulets.

The paper is organized as follows. In Sec. II we summarize the thin film model we use for the study of drop depinning in 3D and introduce the numerical tools we employ. In Sec. III we discuss the results, first for drops and ridges on a horizontal substrate (Sec. III A), and then for ridges on an inclined substrate (Sec. III B), followed by drops and droplike states on an inclined substrate (Sec. III C). We interpret our results in Sec. IV, followed by conclusions in Sec. V.

## II. MODEL AND NUMERICAL TOOLS

### A. Lubrication equation

The partial differential equation governing the time evolution of the profile of a thin liquid film was discussed in depth in the 2D case in Ref. [39] and adapted to the 3D case in Ref. [41]. Briefly, we consider a layer or drop of partially wetting liquid (with a small equilibrium contact angle) on a flat chemically inhomogeneous two-dimensional solid substrate (see sketch in Fig. 1). Long-wave theory allows us to derive an evolution equation for the film thickness profile $h(x,y,t)$ directly from the Navier-Stokes and continuity equations [60,61]. We use no-slip and no-penetration boundary conditions at the substrate, and the equilibrium of tangential and normal stresses at the free surface. The wettability properties are incorporated as a disjoining pressure [2,60]. In the presence of a small (for consistency with the long-wave approximation) lateral body force in the $x$ direction we obtain the nondimensional equation

$$\partial_t h = -\nabla \cdot (Q(h)\{\nabla[\Delta h + \Pi(h,x)] + \mu \mathbf{e}_x\}), \qquad (1)$$

where $\nabla = (\partial_x, \partial_y)$ and $\Delta = \partial_{xx}^2 + \partial_{yy}^2$ are the planar gradient and Laplace operator, respectively, with $(x,y)$ denoting the

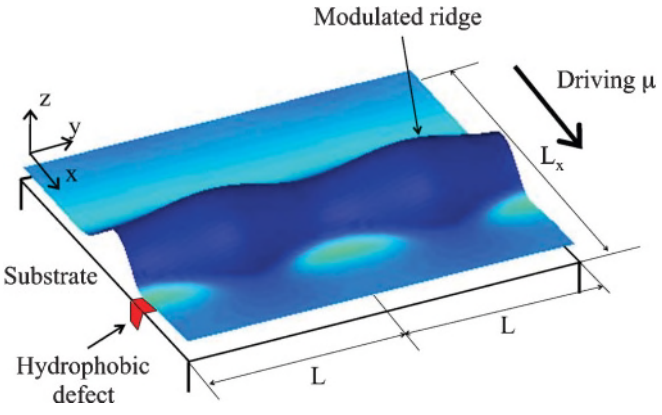


FIG. 1. (Color online) Sketch of the geometry of the problem: A ridge or drop is pinned at a stripelike hydrophobic defect, i.e., a heterogeneous wettability that depends only on the $x$- coordinate. A driving force $\mu$ acts in the $x$- direction.

downstream and spanwise directions. The mobility function $Q(h) \equiv h^3$ corresponds to a parabolic velocity profile (Poiseuille flow). Capillarity is represented by $\Delta h$ (Laplace pressure). The position-dependent wetting properties are incorporated via a $y$-independent disjoining pressure $\Pi(h,x)$ in order to focus on stripelike defects. Of the different functional forms for $\Pi(h)$ found in the literature [2,62], many allow for the presence of a precursor film of thickness 1–10 nm on a "dry" substrate and these are used to describe partial wetting. In this way "true" film rupture in dewetting and the stress singularity at a moving contact line are avoided. Here, we employ long-range apolar van der Waals interactions combined with a short-range polar electrostatic or entropic interaction [2,63,64], leading to the dimensionless disjoining pressure

$$\Pi(h,x) = \frac{b}{h^3} - [1 + \epsilon\xi(x)]\, e^{-h}, \tag{2}$$

where the parameter $b > 0$ indicates the relative importance of the two antagonistic interactions. In the following we employ this particular form of the disjoining pressure with the parameter $b$ fixed at $b = 0.1$ to allow for quantitative comparison with the results of Refs. [39–41] but emphasize that any qualitatively similar disjoining pressure $\Pi$ yields like results, as becomes clear when comparing, for example, the dewetting results in [64–69]. In Eq. (2), $\epsilon$ and $\xi(x)$ are the strength of the wettability contrast and the shape function of the heterogeneity, respectively. For the latter we use a Jacobi elliptic function to model periodic arrays of localized defects, specifically

$$\xi(x) \;=\; 2\{\mathrm{cn}[2\mathrm{K(k)x/L_x,k}]\}^2 - \bar{C}, \tag{3}$$

where $k$ is the modulus of the elliptic function and $K(k)$ is the complete elliptic integral of the first kind. As $k \to 1$ Eq. (3) describes localized defects. Throughout the paper we take $k = (1 - 10^{-6})^{1/2}$ with $\bar{C} = 0.241\,136$ so that $\int_0^{L_x} \xi(x)dx = 0$, i.e., the mean of the disjoining pressure does not depend on the wettability contrast $\epsilon$. In addition, we take the period $L_x$ sufficiently large to avoid interactions between adjacent drops or defects. The resulting wettability profile $\xi(x)$ is shown in Fig. 2(b), lower panel. The wettability contrast $\epsilon > 0$ ($\epsilon < 0$) indicates a hydrophobic (hydrophilic) defect, i.e., it tells us whether the defect is less (more) wettable than the surrounding substrate. Thus $\Pi(h,x)$ allows us to incorporate a stripelike wettability pattern in the theory and to study the influence of chemical substrate heterogeneities or defects via a spatial modulation of the material parameters involved. This variation must take place on length scales much larger than the film thickness for consistency with the long-wave approximation [70].

In nondimensionalizing the model to arrive at Eq. (1) we have used the length scales $l$ for the film thickness and $\sqrt{l\gamma/\kappa}$ for the $(x,y)$ coordinates, the time scale $3\eta\gamma/\kappa^2 l$ for the time, and the force scale $\sqrt{l\gamma}/\kappa^{3/2}$ for the force. The length $l$ corresponds to a characteristic scale for the thickness of the wetting layer, while $\gamma$ and $\eta$ are the surface tension and viscosity of the liquid, respectively; $\kappa$ is a typical energy density scale related to wettability. The ratio of the vertical and horizontal length scales used, $\sqrt{l\kappa/\gamma}$, corresponds to the smallness parameter in the lubrication approximation. This

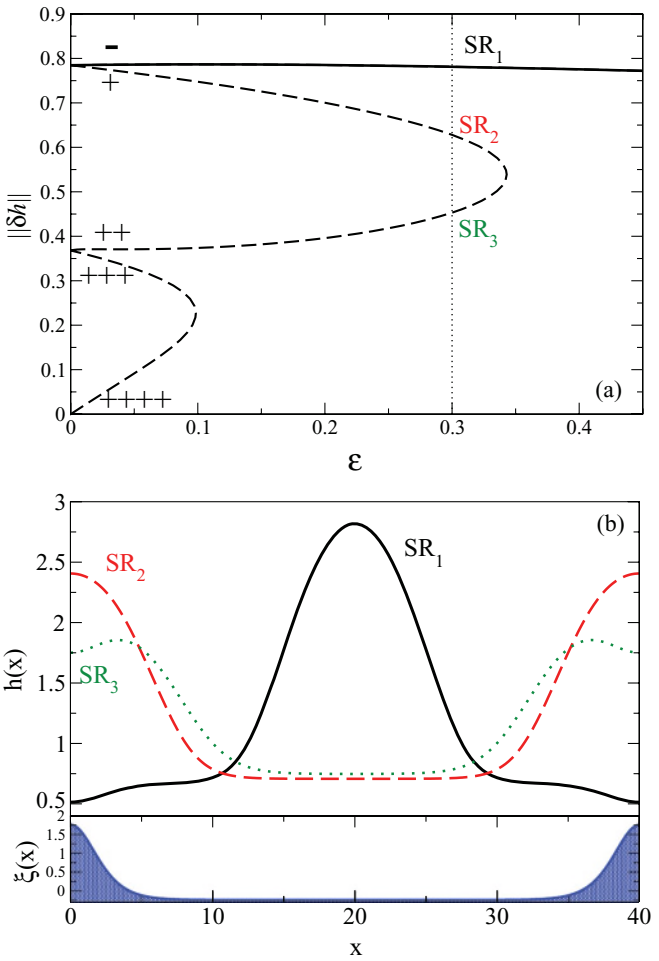


FIG. 2. (Color online) (a) Steady ridge (SR) solutions on a horizontal substrate with hydrophobic line defects as a function of the wettability contrast $\epsilon$. Solid (dashed) lines indicate stable (unstable) solutions. The symbols $\pm$ indicate the stability of the branches w.r.t. 2D perturbations, with $-$ indicating stability and the $+$'s indicating the number of unstable eigenmodes. (b) Profiles of the solutions $SR_1$, $SR_2$, and $SR_3$ at $\epsilon = 0.3$ (top panel) together with the heterogeneity profile $\xi(x)$ (lower panel). Here and in subsequent figures the hydrophobic defect is always centered at $x = 0$ ($x = L$). Parameters: $\bar{h} = 1.2$, $L_x = 40$.

parameter is also closely related to the equilibrium contact angle on a homogeneous substrate; cf. [8]. In writing Eq. (1) we assumed that the lateral driving force, of dimensionless strength $\mu$, does not depend on the film thickness. This is the case for gravitational or centrifugal forces. For driving forces that depend on the film thickness the mobility for the force will differ from that for the pressure term. This is the case for a purely lateral temperature gradient or a gradient of an electric field for a dielectric liquid in a capacitor. Note that the long-wave scaling used here implies that the dimensionless contact angle and driving force $\mu$ may be of order 1.

In the literature one finds two different ways of counting spatial dimensions in the problem at hand. On the one hand, focusing on the mathematical structure of Eq. (1) one distinguishes between one-dimensional ($h$ depends on $x$ only) and two-dimensional ($h$ depends on $x$ and $y$) cases. On the other hand, one may count the physical dimensions

and refer to the situation where the film thickness depends only on $x$ [depends on $(x,y)$] as the two-dimensional (2D) case [three-dimensional (3D) case]. Here we follow the latter convention.

### B. Numerical schemes and parameters

Based on Eq. (1) and the disjoining pressure (2) the 3D depinning behavior is analyzed as follows: Steady-state solutions (pinned drops) and their stability are determined using continuation techniques and the stick-slip motion beyond the depinning threshold is analyzed using time-stepping algorithms. Note that in the 2D case [39,40] an explicit scheme suffices for the latter and continuation can be performed using the package AUTO [71–73]. This is not possible in the 3D case where an accurate and effective time simulation of Eq. (1) remains a challenge, leading to a number of numerical issues [74–76]. For these reasons we employ here an exponential propagation approach based on the exact solution of the linearized equation at each time step [77]. The required exponentiation of the Jacobian matrix is performed using a Krylov reduction based on the Cayley-Arnoldi algorithm [54]. The approach allows for a very good estimate of the optimal time step in both the slow and fast dynamical regimes. This is of paramount importance since close to the depinning transition typical time scales vary over many orders of magnitude. The same Cayley-Arnoldi algorithm is employed in our tangent predictor-secant corrector scheme for the continuation of steady 3D drop states [54]. This approach is advantageous as it allows us to perform all tasks arising in a bifurcation analysis simultaneously. This includes the computation of the kernel of the Jacobian to detect bifurcations and the stability analysis of the steady states.

Steady solutions are characterized by their $L^2$ norm

$$||\delta h|| = \left[\frac{1}{L_x L_y}\int_0^{L_y}\int_0^{L_x}[h(x,y)-\bar{h}]^2\,dxdy\right]^{1/2}, \quad (4)$$

while time-dependent states such as sliding drops or ridges are characterized by their temporal period $T$ and time-averaged norm

$$||\delta h|| = \left[\frac{1}{T}\frac{1}{L_x L_y}\int_0^{T}\int_0^{L_y}\int_0^{L_x}[h(x,y,t)-\bar{h}]^2 dxdydt\right]^{1/2}. \quad (5)$$

In this paper we focus on a regular array of *hydrophobic* stripelike defects with a wettability contrast $\epsilon = 0.3$ with periodic boundary conditions in the downstream direction with period $L_x = 40$ containing a single defect. Periodic boundary conditions are employed in the spanwise direction as well, with period $L_y$ which may be varied to study drops of different volume and spanwise ridges of different length. In these circumstances $L_y$ is used as a bifurcation parameter and is then denoted by the symbol $L$. In this paper the values of $L$ are restricted by the requirement that the domain contains no more than one drop in the spanwise direction. The mean film height is fixed at $\bar{h} = 1.2$, compared with the precursor film height $h = 1$.

## III. RESULTS

### A. Drops and ridges on a horizontal substrate: $\mu = 0$

On a heterogeneous substrate with a periodic array of hydrophobic defects the unique stable solution in the 2D case corresponds to a 2D drop sitting in the middle between two hydrophobic defects [39–41]. In the 3D case this solution corresponds to a ridge with translational invariance in the spanwise direction. Such a ridge may, however, be unstable to a Plateau-Rayleigh instability if the spanwise system size exceeds a critical value $L_c$ as occurs for ridges on homogeneous substrates [57,58]. For cylindrical liquid bridges between two solids the primary bifurcation is an imperfect subcritical pitchfork whose details depend on the particular setting (with/without gravity, thermocapillarity etc.), the mode number, the boundary conditions at the two supports, and their geometry [78,79]. Less is known for a ridge on a solid substrate, where most results [25,26,57,80–82] concern linear stability. For example, ridges on striped heterogeneous substrates can be stabilized with respect to (w.r.t.) the Plateau-Rayleigh instability for any $L_y$ if they sit on a hydrophilic stripe or between hydrophobic stripes of sufficient wettability contrast [26]. In the nonlinear regime we expect to find a (subcritical) pitchfork of revolution (due to translation invariance in the spanwise direction in our periodic setting) when the spanwise system size $L \equiv L_y$ increases. Bulge states with large contact angles are studied in [83].

Figure 2(a) shows the 2D solutions on a horizontal substrate ($\mu = 0$) as a function of the wettability contrast $\epsilon$ and indicates the presence of three 2D states when $\epsilon = 0.3$. The solutions take the form of steady ridges (SRs) of different $L^2$ norm and differ in both the location of the ridge relative to the hydrophobic heterogeneity and their linear stability properties. The largest amplitude solution, labeled $SR_1$, consists of a ridge confined midway between adjacent hydrophobic defects [Fig. 2(b)]; this solution is stable with respect to 2D perturbations. In contrast, the solutions $SR_2$ and $SR_3$ are unstable. Of these, $SR_2$ consists of ridges superposed on top of the defects, a configuration that is expected to be unstable. The lowest amplitude solution $SR_3$ is characterized by minima in the film profile $h(x)$ at both the defects and halfway between them [Fig. 2(b)]. This solution is also unstable.

Figure 3 extends these results to 3D structures on a horizontal substrate ($\mu = 0$). To obtain the figure we start with a stable $SR_1$ solution in Fig. 2 with either $\epsilon = 0$ (homogeneous substrate) or $\epsilon = 0.3$ (hydrophobic line defect) and study its linear stability with respect to 3D volume-conserving perturbations with period $L$ in the spanwise direction. A symmetry-breaking Plateau-Rayleigh-like instability sets in for $L > L_{c1}^0$ (the superscript zero refers to $\mu = 0$, i.e., the absence of a driving force). At $L_{c1}^0$ a branch of steady 3D solutions bifurcates from the 2D states when an eigenvalue of double multiplicity becomes unstable. The double multiplicity is a consequence of O(2) symmetry of the SR stability problem under translations in $y$ modulo the period $L$ together with the reflection $y \to -y$ and is not indicated in Fig. 3 or subsequent figures. The 3D solutions that result take the form of unstable ridges modulated in the spanwise direction [see Fig. 4(b)]. With increasing modulation amplitude these solutions turn around at a saddle-node bifurcation

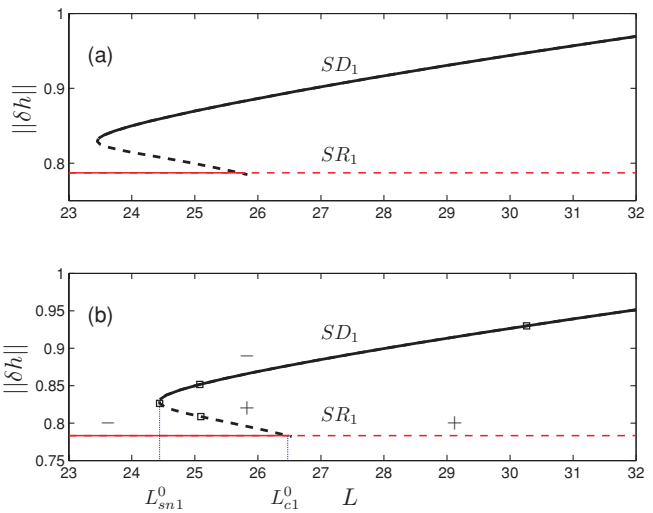


FIG. 3. (Color online) Bifurcation diagrams for (a) $\epsilon = 0$ and (b) $\epsilon = 0.3$ showing the loss of stability of the $SR_1$ solutions (horizontal red line) with respect to 3D perturbations when the spanwise period $L$ increases together with the resulting branch of 3D states labeled $SD_1$ (black line). Solid (dashed) lines indicate stable (unstable) solutions. Solution profiles at locations indicated by open squares in (b) are shown in Fig. 4. Parameters: $\mu = 0$, $\bar{h} = 1.2$, $L_x = 40$.

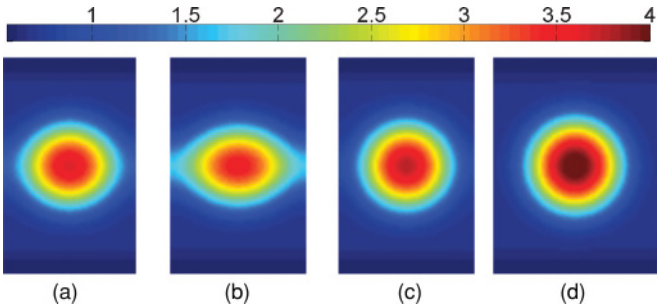


FIG. 4. (Color online) Steady droplike states $SD_1$ at locations indicated by open squares in Fig. 3(b) in terms of contours of constant $h(x,y)$. (a) The saddle-node bifurcation at $L^0_{sn1} = 24.44$, (b) the unstable branch at $L = 25.09$, (c) the stable branch at $L = 25.08$, and (d) $L = 30.26$. The downslope direction $x$ is from top to bottom, with $y$ horizontal. Parameters: $\mu = 0$, $\epsilon = 0.3$, $\bar{h} = 1.2$, $L_x = 40$.

(at $L = L^0_{sn1}$) and acquire stability. At approximately the same location the solution ceases to resemble a spatially modulated ridge and begins to resemble a steady droplike (SD) state. In the following we use the notation SD to refer to all 3D states, even near the bifurcation $L^0_{c1}$, where their appearance is ridgelike. It follows that for $L < L^0_{sn1}$ the only stable solution is the 2D ridge state $SR_1$ that is invariant w.r.t. spanwise translations. For $L > L^0_{c1}$ the ridge is linearly unstable and decays into the drops $SD_1$ that constitute the only stable solution in this regime. In between, i.e., in the range $L^0_{sn1} < L < L^0_{c1}$, both the $SR_1$ and the larger-amplitude $SD_1$ solutions are linearly stable, while the unstable subcritical $SD_1$ branch of modulated ridges corresponds to unstable threshold solutions separating the two stable solutions. Comparison of Figs. 3(a) and 3(b) shows that presence of the defect shifts the bifurcation to 3D states and the saddle-node bifurcation on the resulting branch of 3D states to larger values of the parameter $L$ than required for the Plateau-Rayleigh instability on a homogeneous substrate. In fact, this stabilizing effect is much more pronounced in the hydrophilic case ($\epsilon < 0$, not shown).

Figure 4 shows a sequence of solutions along the $SD_1$ branch of 3D states created at $L^0_{c1}$ when $\mu = 0$, corresponding to locations indicated by open squares in Fig. 3(b), i.e., for $\epsilon = 0.3$. Figure 4(a) shows the solution at the saddle node ($L^0_{sn1} = 24.44$), with Fig. 4(b) showing the unstable ridgelike state below the saddle node ($L = 25 < L^0_{c1} = 26.6$) and Fig. 4(c) showing the corresponding stable droplike state above the saddle node, at the same value of $L$. Figure 4(d) shows the (stable) drop state at $L = 30 > L^0_{c1}$. We emphasize that the notion of stability is limited to linear stability with respect to perturbations with spatial period $L$. It turns out that the large amplitude drop branch is typically unstable w.r.t. coarsening, i.e., to perturbations with periods that are integer multiples of $L$. However, we do not pursue questions related to coarsening in the present work.

Figure 5 shows, in addition to the $SD_1$ states, four additional branches of droplike states. Of these the states labeled $SD_2$ and $SD_3$ lie on a pair of unstable branches that are connected via a common saddle-node bifurcation at $L_{sn2} \approx 25.0$ but that are disconnected from the ridge states $SR_1$, $SR_2$, and $SR_3$ (Fig. 5). The states labeled $SD_2$ consist of drops sitting on the defect with a maximum on the defect while $SD_3$ consist of drops sitting on the defect with maxima on either side of the defect [Figs. 6(a) and 6(b)], just as for the

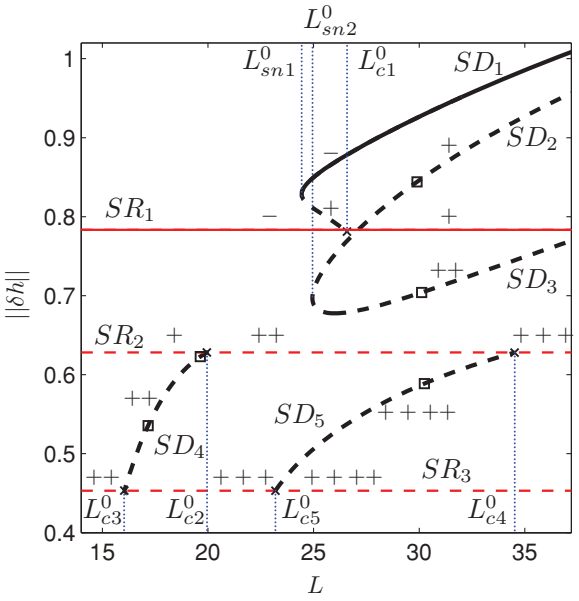


FIG. 5. (Color online) Bifurcation diagram showing secondary bifurcations to 3D states from the branches $SR_1$, $SR_2$, and $SR_3$ (horizontal red lines) of 2D steady ridges, and the associated branches of 3D steady droplike states $SD_1$, $SD_2$, $SD_3$, and $SD_4$ (heavy black lines). Solid (dashed) lines indicate stable (unstable) solutions. Solution profiles at locations indicated by open squares are shown in Fig. 6. Parameters: $\mu = 0$, $\epsilon = 0.3$, $\bar{h} = 1.2$, $L_x = 40$.

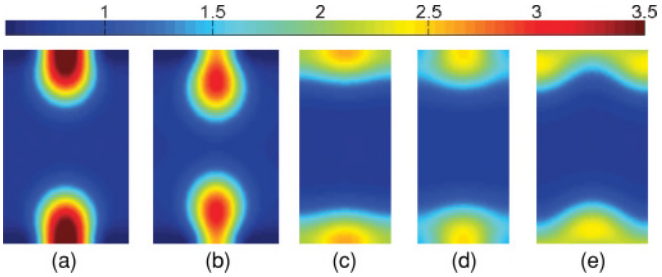


FIG. 6. (Color online) Steady droplike states at locations indicated by open squares in Fig. 5 in terms of contours of constant $h(x,y)$. (a) $SD_2$ at $L = 29.90$, (b) $SD_3$ at $L = 30.11$, (c) $SD_4$ at $L = 19.64$ (close to $SR_2$), (d) $SD_4$ at $L = 17.17$ (close to $SR_3$), and (e) $SD_5$ at $L = 30.25$. The downslope direction $x$ is from top to bottom, with $y$ horizontal. Parameters: $\mu = 0, \epsilon = 0.3, \bar{h} = 1.2, L_x = 40$.

corresponding $SR_2$ and $SR_3$ states. In addition, we find two further branches of droplike states, hereafter $SD_4$ and $SD_5$, both created as a result of symmetry-breaking bifurcations of the $SR_2$ and $SR_3$ states. Following [84] we refer to these states as varicose and zigzag states. The former are shown in Figs. 6(c) and 6(d) at two locations along the $SD_4$ branch; the latter solution is shown in Fig. 6(e). As shown in Fig. 5 the varicose (zigzag) branch bifurcates subcritically from $SR_2$ at $L^0_{c2} = 19.95$ ($L^0_{c4} = 34.52$) and connects to $SR_3$ supercritically at $L^0_{c3} = 16.05$ ($L^0_{c5} = 23.19$). Note that the $SD_4$ branch is twice unstable while the $SD_5$ branch is four times unstable. As explained in [84] this is a consequence of the fact that the zigzag state is unstable with respect to two different varicose modes. Technically, the unstable eigenvalue of double multiplicity splits into two eigenvalues when moving from the SR branch onto the $SD_5$ branch.

### B. Ridge on an inclined substrate: $\mu > 0$

Once the driving force $\mu$ becomes nonzero, the ridge or drop solutions will be displaced from their symmetric location midway between a pair of hydrophobic defects. This is a consequence of the term $-\mu\partial_x Q(h)$ in Eq. (1) that breaks the reflection symmetry in the $x$ direction. On a homogeneous substrate the solutions acquire an asymmetric shape w.r.t. $x \to -x$ and slide downstream like a solitary wave of constant shape [5,85]. On a heterogeneous substrate, however, the wettability defect may pin such a sliding solution depending on the relative size of the parameters $\mu$ and $\epsilon$. In the present case of a hydrophobic defect with $\epsilon = 0.3$ the ridge or drop will be blocked at its front. A finite force $\mu > \mu_{\rm depin}$ is needed to overcome the pinning effect of the defect in order that the ridge or drop may move. Beyond this depinning transition ridges or drops slide along the plane but do so with a nonuniform speed since both their shape and speed are modulated periodically as they pass individual defects in the periodic defect array [39–41]. In 2D the depinning itself is either related to a saddle-node infinite period (sniper) bifurcation or to a Hopf bifurcation. As already mentioned the sniper bifurcation generates stick-slip motion just above $\mu_{\rm depin}$ since the ridge sticks for a long time to a defect before sliding to the next one [40].

In this section we seek to elucidate the depinning process for 3D drops and relate it to the corresponding process in 2D. We begin with stability and depinning of the 2D SR states.

#### 1. Depinning in two dimensions

Figure 7(a) presents the bifurcation diagram for $\epsilon = 0.3$ (hydrophobic defects) as a function of the driving force $\mu$ obtained using numerical continuation and direct numerical simulation in time. The figure shows 2D states only, with the $L^2$ norm (4) for steady ridges and the time-averaged $L^2$ norm (5) for the stick-slip states (SSRs). As soon as $\mu \neq 0$ the profiles of the SR states become markedly asymmetric as shown for $SR_1$ in Fig. 7(c). The figure illustrates the dramatic shift in the position of the dominant maximum of the solution toward the downstream defect arising from the competition between the driving force and the blocking effect of the defect that prevents downstream motion. As the driving force $\mu$ increases the ridge profile steepens [i.e., the norm (4) increases]. However, close to the saddle-node bifurcation at $\mu = \mu^{\rm 2d}_{\rm sn1} \approx 0.011\,57$ the norm starts to decrease, and for the parameters used the saddle-node bifurcation is preceded by a Hopf bifurcation at $\mu^{\rm 2d}_{\rm Hopf} \approx 0.011\,54$ [Fig. 7(c)]. This bifurcation leads to a subcritical branch of unstable small amplitude time-periodic "rocking" states hereafter referred to as oscillating ridges (ORs). We conjecture that with decreasing $\mu$ these states undergo a global bifurcation to translating states at some $\mu = \mu^{\rm 2d}_g$ ($\mu^{\rm 2d}_g < \mu^{\rm 2d}_{\rm Hopf} < \mu^{\rm 2d}_{\rm sn1}$). These states differ, however, from the usual stick-slip states generated via the sniper bifurcation since the ridge must spend considerable time in the rocking state before shifting rapidly to the next defect downstream.

Figure 7(b) zooms into the region of the bifurcation diagram where stable stick-slip ridges are present, while Figs. 8 and 9 show several of these states as a function of time over one period $T$ in terms of space-time plots (Fig. 8) and $L^2$ norm (Fig. 9). Here the "period" refers to the time required for the ridge to slide from one defect to the next. Figure 7(b, inset) suggests that the period $T$ diverges logarithmically as $\mu \to \mu_g$ as expected from a global bifurcation. Examination of the SSR profile near $\mu = \mu_g$ when it is almost pinned suggests that the SSR approaches a profile close to an $SR_1$ on the intermediate segment of the $SR_1$ branch (not shown). The leading eigenvalues along the $SR_1$ branch are shown in Fig. 7(d) with the heavy red lines indicating the eigenvalues along the intermediate segment. For $\mu \approx \mu_g$ the states on this segment have a single unstable eigenvalue $\lambda_u \approx 0.0101$ and a leading stable eigenvalue $\lambda_s \approx -0.000\,54$. Thus $\lambda_u + \lambda_s > 0$ and under these conditions standard theory shows that any global bifurcation involving states on the intermediate segment of the $SR_1$ branch must involve *unstable* periodic states (see the 3D case below for further discussion). This conclusion is consistent with the behavior of the SSR norm [Fig. 7(b)] which suggests that the SSR states do indeed undergo a saddle-node bifurcation prior to any global bifurcation and so are unstable near $\mu = \mu_g$.

The leading eigenvalues on the intermediate segment of $SR_1$ are created by the collision on the positive real axis of the unstable complex eigenvalues responsible for the Hopf bifurcation on the upper segment of the $SR_1$ branch. After this

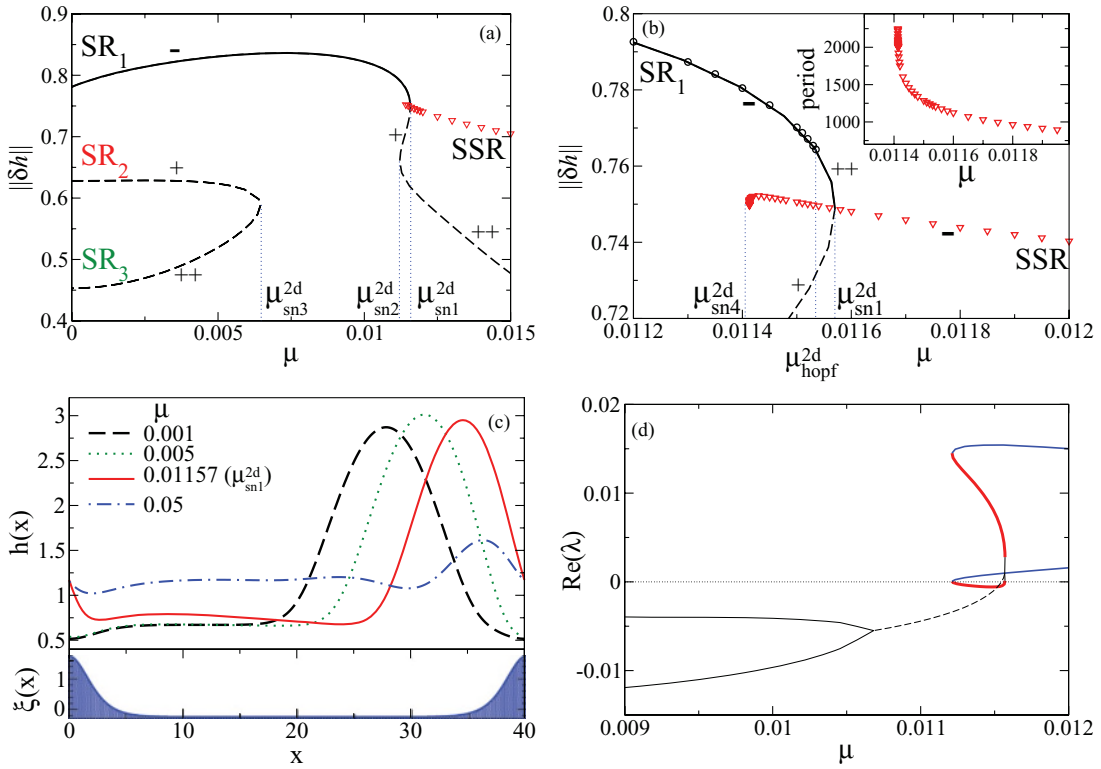


FIG. 7. (Color online) (a) Bifurcation diagram showing the amplitude of the three steady 2D states identified in Fig. 2 as a function of $\mu$. Solid (dashed) lines indicate solutions that are stable (unstable) with respect to perturbations with a real eigenvalue. At larger $\mu$ only $SR_1$ exists. The open triangles indicate solutions on the branch of stable stick-slip ridges (SSR). (b) Zoom of (a) showing the SSR branch in greater detail; the inset shows the time taken to travel between successive defects, also as a function of $\mu$. The open circles denote solutions that are stable with respect to oscillations. The symbols $\pm$ indicate the stability of the branches w.r.t. 2D perturbations, with $-$ indicating stability and the $+$'s indicating the number of unstable eigenmodes. (c) Solution profiles along the upper $SR_1$ branch showing the blocking of the ridge by the downstream defect (the driving force acts toward the right). (d) The real part of the leading eigenvalues of the $SR_1$ states as a function of $\mu$. The solid (dashed) lines correspond to real (complex) eigenvalues. The three different linewidths correspond to the three sub-branches separated by saddle-node bifurcations. Parameters: $\epsilon = 0.3$, $\bar{h} = 1.2$, $L_x = 40$.

collision the eigenvalues remain real with one continuing to increase as one follows the branch while the other crosses back into the negative half plane at the saddle node $\mu^{2d}_{sn1}$. At this point the steady branch turns back toward smaller $\mu$ [Fig. 7(b)]. The bifurcation at $\mu^{2d}_{sn1}$ is a standard saddle-node bifurcation and not a sniper. This is because for the parameter values used the depinning transition involves the unstable OR states instead of the $SR_1$ states, i.e., with the appearance of the Hopf bifurcation the depinning transition moves from the steady states $SR_1$ to the time-dependent OR states. At a further saddle node at $\mu^{2d}_{sn2} \approx 0.0112$ the branch turns again toward increasing $\mu$, now with two unstable real eigenvalues [Fig. 7(c)]. With further increase in $\mu$ the $L^2$ norm of these unstable states continues to decrease as the solution begins to resemble more and more a steady 2D flowing film whose profile is modulated by the hydrophobic defects in the substrate below.

Since each of the three SR states at $\mu = 0$ can itself be continued in $\mu$ we expect to find additional SR states when $\mu > 0$. Of these $SR_2$ and $SR_3$ annihilate in a saddle-node bifurcation at $\mu^{2d}_{sn3} \approx 0.0065$ [Fig. 7(a)] leaving only the state $SR_1$ at larger $\mu$. These states play no role in the depinning transition and the bifurcation at $\mu^{2d}_{sn3}$ is a regular saddle-node bifurcation.

For larger ridge volumes (e.g., $\bar{h} = 1.3$) the bifurcation diagram simplifies since the Hopf bifurcation is now absent. In this case the branch of stick-slip ridges emerges directly from the saddle-node bifurcation in a sniper bifurcation, as confirmed by the fact that the inverse time period now varies as $(\mu - \mu^{2d}_{sn1})^{1/2}$ near the bifurcation. For a more detailed discussion of the transition between these two scenarios, see Ref. [39].

### 2. *Transverse instability of a ridge*

A real 3D system will, however, show the behavior described in the previous section only if the spanwise domain size $L$ is small. For large or indeed infinite $L$ the ridge solutions (2D drops) are unstable, as already noted, with respect to spanwise perturbations. On a horizontal substrate ($\mu = 0$) the only relevant instability of this type is the Plateau-Rayleigh instability discussed in Sec. III A. In this section we discuss analogous instabilities when $\mu > 0$.

To do so we follow the $SR_1$ branch in Fig. 7(a) as a function of $\mu$ together with the eigenvalues determining its linear stability properties with respect to spanwise perturbations of spatial period $L$. This procedure allows us to identify,

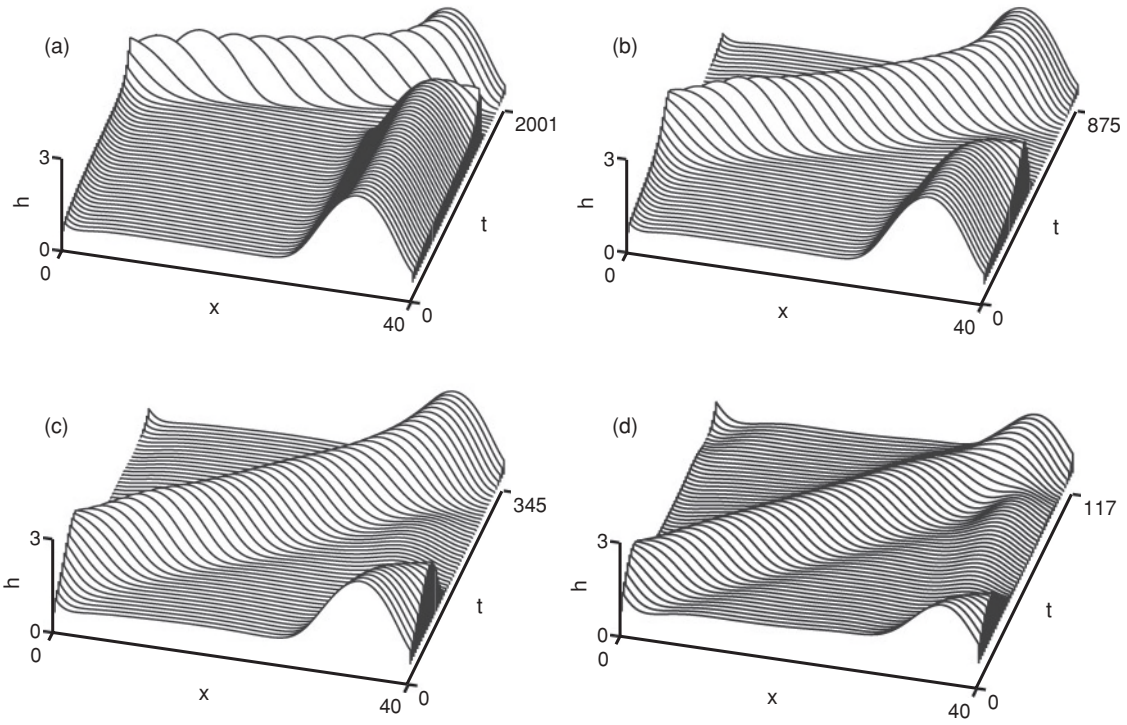


FIG. 8. Space-time plots of the time evolution of stick-slipping ridge (SSR) solutions beyond depinning via a Hopf bifurcation over one period in space and time at (a) $\mu = 0.011\,414$ close to the saddle node of the SSR branch at $\mu_{\rm sn4}^{\rm 2d} = 0.011\,413\,03$ with temporal period $T = 2000.6$, (b) $\mu = 0.012$ with $T = 875.0$, (c) $\mu = 0.02$ with $T = 345.0$, and (d) far from depinning, $\mu = 0.06$ with $T = 116.8$.

as a function of $\mu$, the critical spanwise domain size $L_c$ for the onset of a linear instability. The underlying linear stability analysis is performed using the ansatz $h(x,y) = h_0(x) + \alpha h_1(x)\exp(ik_y y)$ with $k_y = 2\pi/L$.

The resulting stability diagram in the $(L,\mu)$ plane is shown in Fig. 10. Figure 11 shows four sample perturbation profiles $h_1(x)$ along the stability boundary together with the associated ridge profiles $h_0(x)$. These are discussed below.

On the horizontal substrate ($\mu = 0$) the $SR_1$ states are stable below the critical length $L_{c1}^0$. When $\mu > 0$ these states become asymmetric with respect to the reflection $x \to -x$ [Fig. 7(c)] but remain stable for $\mu < \mu_{c1}^{\rm 3d}(L)$. For $L_{c1}^0 < L < L_{\rm max}$ the $SR_1$ states are stable or unstable depending on the value of

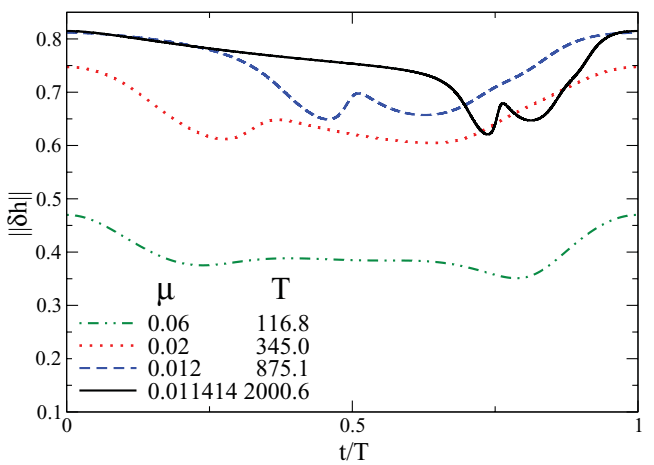


FIG. 9. (Color online) The $L^2$ norm as a function of time for selected solutions on the branch of stick-slip ridges (SSRs). Time is scaled by the period $T$ listed in the legend together with the corresponding values of $\mu$.

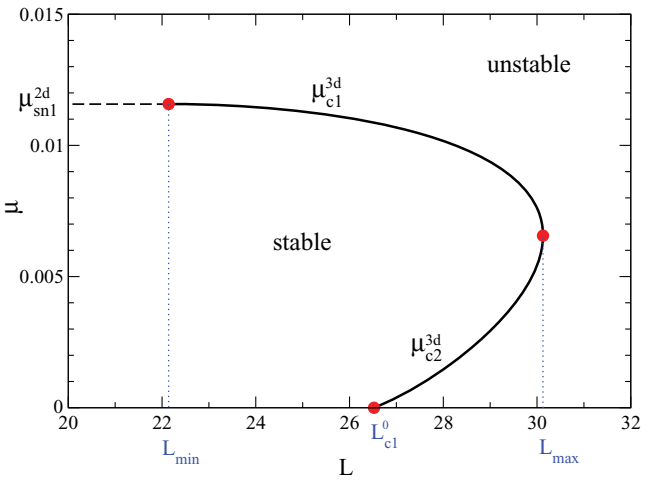


FIG. 10. (Color online) Stability diagram for steady ridge states on a heterogeneous incline showing the region of linear stability in the $(L,\mu)$ plane. Solid (dashed) lines indicate the presence of 3D (2D) instability. The remaining parameters are as in Fig. 7.

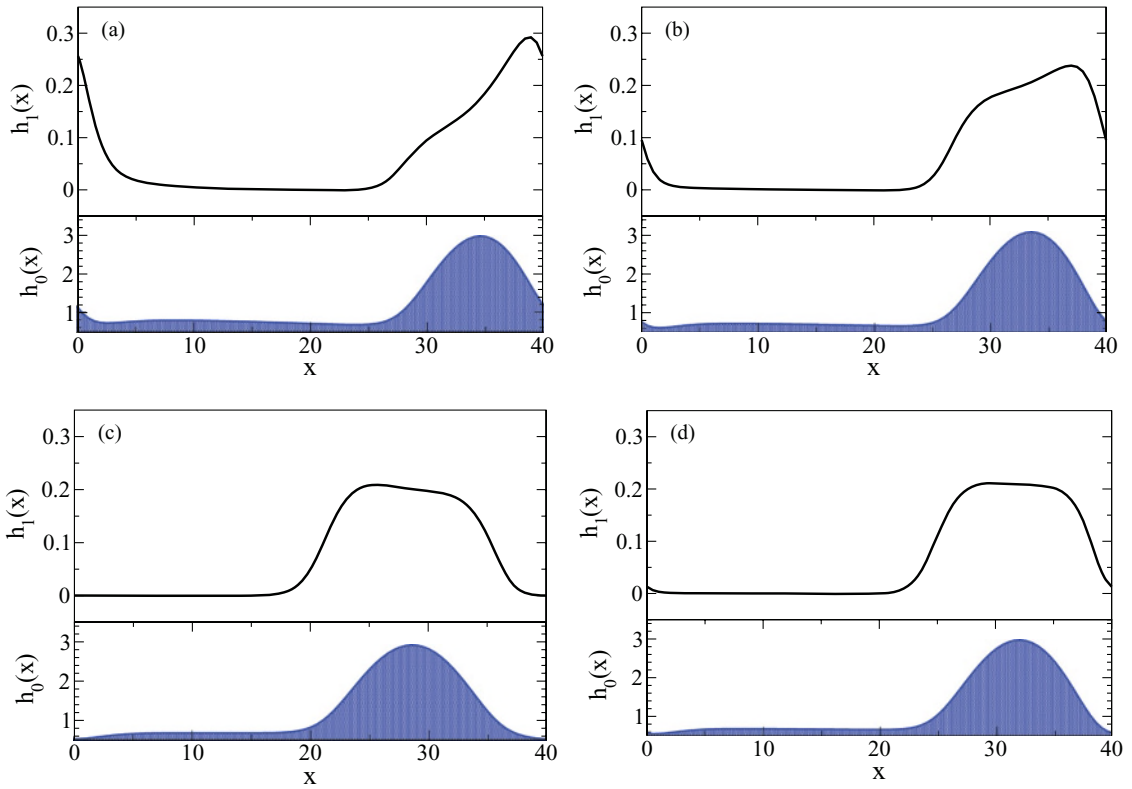


FIG. 11. (Color online) The marginal eigenfunctions $h_1(x)$ along the stability boundary in Fig. 10 (upper panels) and associated steady ridge profiles $h_0(x)$ (lower panels) at (a) $\mu = 0.011\,57$, $L = 22.5$; (b) $\mu = 0.010\,19$, $L = 28.0$; (c) $\mu = 0.001\,47$, $L = 28.0$; (d) $\mu = 0.006\,56$, $L_{\max} = 30.1$.

$\mu$. This is a consequence of the nonmonotonic dependence of $L_{c1}$ on $\mu$ shown in Fig. 10 for $\epsilon = 0.3$: the value of $L_{c1}$ first increases from $L_{c1}^0$ to a maximum value $L_{\max}$ at $\mu_{\max}$ before decreasing toward $L_{\min}$ at $\mu_{\rm sn1}^{\rm 2d}$. For the present parameter values $L_{\min} < L_{c1}^0$ and linear considerations alone allow one to distinguish four qualitatively different responses to the driving force $\mu$, depending on the lateral system size $L$:

(i) For $L \leqslant L_{\min} = 22.4$ the pinned ridge is linearly stable with respect to spanwise perturbations in its entire range of existence, i.e., for all $\mu < \mu_{\rm sn1}^{\rm 2d}$. The depinning behavior corresponds to the 2D case.

(ii) For $L_{\min} < L < L_{c1}^0$ the ridge is linearly stable when $\mu = 0$ but loses stability at a driving force $\mu_{c1}^{\rm 3d} < \mu_{\rm sn1}^{\rm 2d}$. The instability has largest amplitude on the downstream side of the ridge [Fig. 11(a)] indicating the onset of spanwise modulations that invade the wettability defect. As $L$ approaches $L_{\min}$, $\mu_{c1}^{\rm 3d}$ approaches $\mu_{\rm sn1}^{\rm 2d}$.

(iii) For $L_{c1}^0 < L < L_{\max}$ the $SR_1$ state is linearly unstable even when $\mu = 0$. Increasing $\mu$ stabilizes the ridge at a critical value $\mu_{c2}^{\rm 3d}$. The marginal eigenfunction [Fig. 11(c)] peaks slightly on the upstream side of the ridge, indicating stabilization with respect to the Plateau-Rayleigh instability. The ridge is then linearly stable up to the critical value $\mu_{c1}^{\rm 3d}$, where it loses stability as in case (ii); cf. Figs. 11(a) and 11(b).

(iv) For $L > L_{\max} = 30.7$ the ridge is linearly unstable for all $\mu$. However, linear analysis is not able to tell whether the ridge will evolve into steady pinned drops or sliding drops. We expect that a critical $\mu$ exists below (above) which the former (latter) occurs.

The different types (i)–(iv) of linear behavior inevitably result in different nonlinear behavior. For example, in cases (ii) and (iii) depinning occurs in an intrinsically 3D manner, as individual "fingers" extend across the defect. Thus the $SR_1$ state does not slide over the defect as a whole. In the following section we analyze the relation between drop and ridge solutions in the parameter regions (i) to (iv). We find that the intricate nonlinear behavior that results requires the introduction of several qualitatively different subregions in parameter space. These are discussed in detail in the next section before an overview of all stable solutions is given in Sec. III D.

### C. Depinning of drops and ridges on an inclined substrate

The analysis of the linear stability of the steady ridge solutions for different spanwise system sizes performed in the previous section indicates that the relation between drop and ridge solutions changes with lateral system size, i.e., with drop volume. The linear analysis allowed us to distinguish four parameter regimes. The curve of neutral stability w.r.t. harmonic spanwise perturbations in Fig. 10 indicates the loci of bifurcation points where modulated ridge solutions emerge from the spanwise-invariant ridges. In the following, we continue these modulated ridge solutions for several fixed values of $L$ while changing $\mu$. In addition, we continue the steady droplike states present at $\mu = 0$ (Sec. III A, Fig. 5) toward larger $\mu$. All solutions obtained in this way are presented in a sequence of bifurcation diagrams together with

the spanwise-invariant ridge solutions. These show branches of time-periodic solutions, i.e., drops and ridges that either oscillate or slide from defect to defect, in addition to the steady solutions.

#### 1. Scenario (i): $L \leqslant L_{\min}$

For $L \leqslant L_{\min}$ the pinned ridge is linearly stable w.r.t. spanwise perturbations and depins via a Hopf bifurcation at $\mu^{2d}_{\rm Hopf} < \mu^{2d}_{\rm sn}$. The marginally stable eigenfunction at the Hopf bifurcation remains translation invariant in the spanwise direction. Consequently the depinning scenario in this case is identical to that already described for the 2D case in Sec. III B 1 and summarized in Fig. 7. After depinning the ridge undergoes stick-slip motion as described for 2D drops in Refs. [39,40]. Depending on the value of $L \leqslant L_{\min}$ this 2D time-dependent state may in turn become unstable to three-dimensional perturbations at some $\mu > \mu^{2d}_{\rm sn4}$, resulting in a sliding 3D state.

The secondary branch $SD_4$ present on the horizontal substrate for $L^0_{c3} < L < L^0_{c2} < L_{\min}$ (Fig. 5) plays no role in any of the depinning scenarios discussed below. Continuation in $\mu$ shows that this solution terminates on either $SR_2$ or $SR_3$, depending on the value of $L$ (Fig. 12). The $SD_5$ solution likewise plays no significant role despite its presence in most of the scenarios discussed below (cf. Figs. 15 and 25 below).

#### 2. Scenario (iia): $L_{\min} \leqslant L \leqslant L^0_{\rm sn1}$

For $L_{\min} \leqslant L \leqslant L^0_{c1}$ the pinned ridge $SR_1$ is linearly stable w.r.t. spanwise perturbations at small $\mu$ but becomes unstable w.r.t. 3D perturbations at some $\mu^{3d}_{c1}(L) < \mu^{2d}_{\rm sn1}$. Thus the Hopf bifurcation that produces depinning may be preceded by a steady-state spanwise instability. In this case the depinning that takes place at larger $\mu$ corresponds to an instability of a 3D steady state.

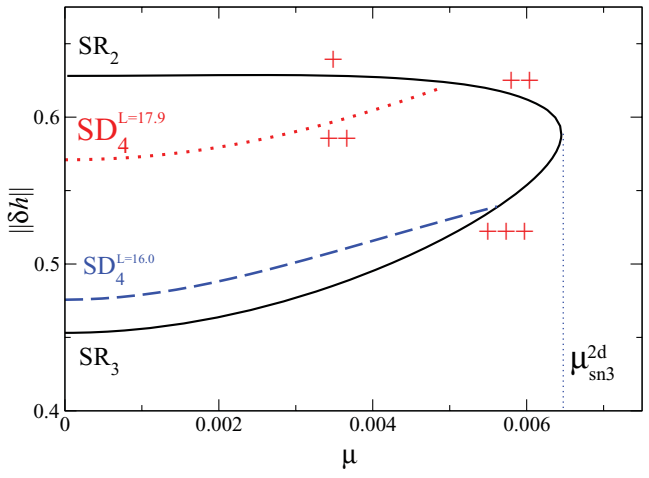


FIG. 12. (Color online) Bifurcation diagram showing the $L^2$ norm $||\delta h||$ of steady solutions $SR_2$ and $SR_3$ as a function of the driving force $\mu$ together with the bifurcating transversally modulated ridges $SD_4$. The latter branch is shown for the two different values $L = 17.9$ (red dotted) and $L = 16.0$ (blue dashed). The number of red $+$'s indicates the number of unstable eigenmodes when $L = 17.9$. Remaining parameters are as in Fig. 2.

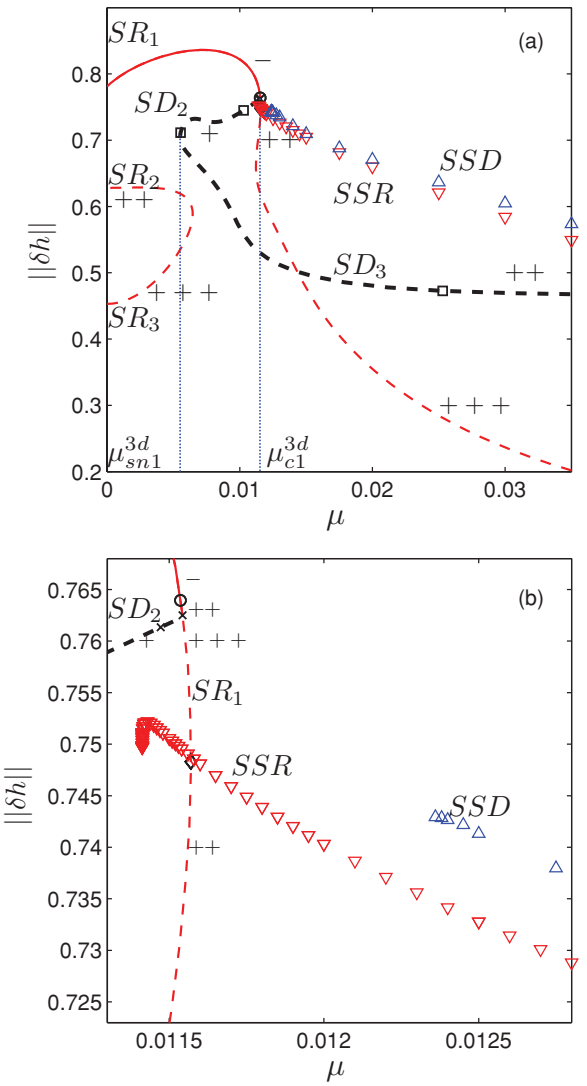


FIG. 13. (Color online) Scenario (iia): (a) Bifurcation diagram for ridge and drop solutions on a substrate with hydrophobic line defects (wettability contrast $\epsilon = 0.3$) and spanwise system size $L_{\min} < L = 23 < L^0_{\rm sn1}$ showing the $L^2$ norm $||\delta h||$ of steady solutions as a function of the driving force $\mu$. A zoom is given in (b). Both steady spanwise-invariant ridges (SR, thin red lines), and secondary drop solutions ($SD_2$ and $SD_3$, black lines) are included. Solid (dashed) lines indicate linearly stable (unstable) solutions. Downward (upward) pointing triangles indicate SSR (SSD) solutions. The former are taken from Fig. 7(b) and are stable with respect to 3D perturbations for $\mu < 0.015$ only. The open circle indicates the location of the Hopf bifurcation, while the square symbols indicate solutions whose profiles are shown in Fig. 14. The $SD_3$ branch acquires stability at $\mu^{3d}_{\rm Hopf} \approx 0.092$ (off scale). The remaining parameters are as in Fig. 3.

We have already seen that when $\mu = 0$ and $L < L^0_{\rm sn1}$ we have the three SR solutions shown in Fig. 7. For $L^0_{\rm sn1} < L < L^0_{c1}$ we have in addition two 3D solutions, one ridgelike and the other droplike. Each of these solutions extends smoothly to $\mu > 0$ with both $L_{\rm sn1}$ and $L_{c1}$ changing with $\mu$, with $L_{\rm sn1}(\mu) < L^0_{\rm sn1}$. Thus for $L_{\min} \leqslant L \leqslant L^0_{\rm sn1}$ the bifurcation diagram takes the form shown in Fig. 13.

Here the branch of largest norm (thin line) corresponds to the steady spanwise-invariant ridges $SR_1$. This solution loses

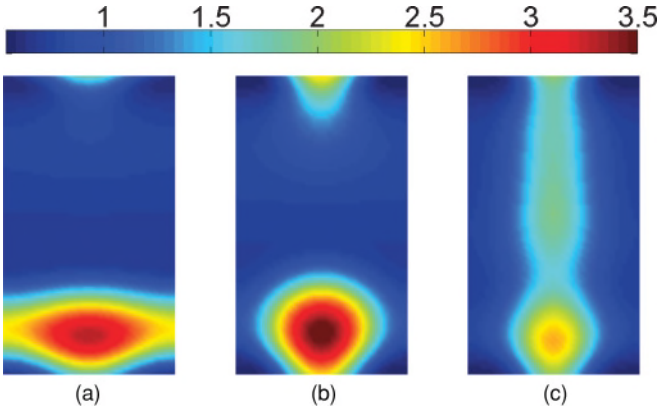


FIG. 14. (Color online) Scenario (iia): Unstable steady states at locations indicated by open squares in Fig. 13 in terms of contours of constant $h(x,y)$. (a) Drop solution $SD_2$ at $\mu = 0.0105$ resembling a modulated ridge. (b) $SD_2$ solution very close to the saddle node at $\mu^{3d}_{sn1} \approx 0.005\,532$. (c) Static rivulet $SD_3$ at $\mu = 0.0253$. Parameters are as in Fig. 13.

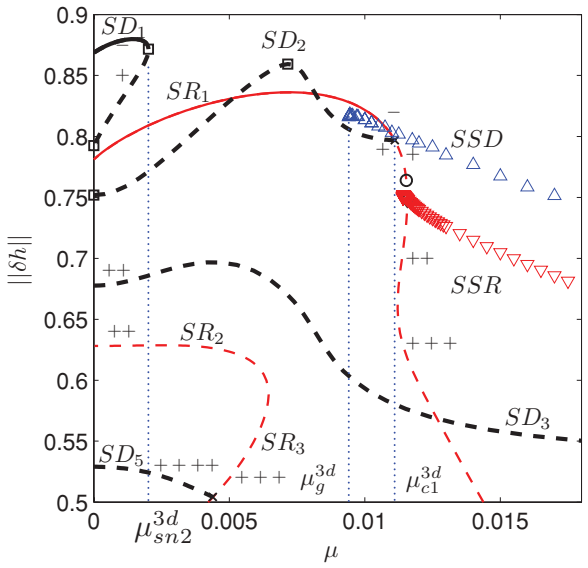


FIG. 15. (Color online) Scenario (iib): Bifurcation diagram for ridge and drop solutions on a substrate with hydrophobic line defects (wettability contrast $\epsilon = 0.3$) and spanwise system size $L = 26$ showing the $L^2$ norm $||\delta h||$ of steady solutions as a function of the driving force $\mu$. Both steady spanwise-invariant ridges ($SR_1$, thin red lines), and secondary drop solutions ($SD_1$, $SD_2$, $SD_3$, and $SD_5$, black lines) are included. Solid (dashed) lines indicate linearly stable (unstable) solutions. Downward (upward) pointing triangles indicate SSR (SSD) solutions. Solution profiles at locations indicated by open squares are shown in Fig. 16. The remaining parameters are as in Fig. 3.

stability with respect to 3D perturbations at $\mu^{3d}_{c1} \approx 0.011\,55$. This value is slightly larger than $\mu^{2d}_{hopf} \approx 0.011\,54$, implying that the $SR_1$ state depins via 2D depinning. The 3D steady states produced at $\mu^{3d}_{c1}$ bifurcate toward smaller $\mu$ before turning around toward larger $\mu$ at a saddle-node bifurcation at $\mu^{3d}_{sn1} \approx 0.005\,532$ and are unstable throughout. In the following we use $SD_2$ to refer to the solutions above the saddle node and $SD_3$ to refer to those below. As shown in Fig. 14 the appearance of the 3D solutions changes substantially along the branch. Near $\mu^{3d}_{c1}$ [Fig. 14(a)] the solution is ridgelike. At the saddle node at $\mu^{3d}_{sn1}$ it becomes droplike [Fig. 14(b)] while at large $\mu$ the solution becomes a steady (unstable) streamwise-modulated rivulet [Fig. 14(c)].

As already mentioned the 2D $SR_1$ state loses stability at $\mu = \mu^{2d}_{Hopf}$ with respect to 2D oscillations (see Sec. III B 2, Fig. 7) and these must undergo a global bifurcation resulting in depinning (Sec. IV). The resulting SSR state remains stable for a range of values of $\mu$ but loses stability at $\mu \approx 0.02$ to spanwise perturbations, resulting in a hysteretic transition to stable stick-slip drops (SSDs). The latter appear to undergo a saddle-node bifurcation near $\mu = 0.0123$ and do not reach any of the steady states at lower $\mu$.

The unstable steady rivulet states on the $SD_3$ branch [Fig. 14(c)] stabilize through a Hopf bifurcation at a much larger $\mu$, $\mu^{3d}_{Hopf} \approx 0.092$. If a time simulation is done for $\mu < \mu^{3d}_{Hopf}$ (but above $\mu \approx 0.01$) with the unstable steady rivulet solution as the initial condition, the rivulet decays into sliding drops corresponding to a state on the SSD branch. Thus the SSD branch terminates in a Hopf bifurcation on the $SD_3$ branch (cf. Fig. 25 below).

### 3. Scenario (iib): $L^0_{sn1} \leqslant L \leqslant L^0_{c1}$

For $L > L^0_{sn1}$ two 3D solutions are present (in addition to the previously studied 2D SR solutions) even at $\mu = 0$. Another two appear at $L = L^0_{sn2}$ slightly above $L^0_{sn1}$ (cf. Fig. 5). The resulting bifurcation diagram is shown in Fig. 15. As in scenario (iia), the pinned 2D ridge is linearly stable at small $\mu$ but becomes unstable w.r.t. 3D perturbations at $\mu^{3d}_{c2}(L) < \mu^{2d}_{Hopf} < \mu^{2d}_{sn1}$. Continuation of the branch of $SD_2$ solutions when $L = 26$ shows a branch that bifurcates subcritically from the $SR_1$ branch at $\mu^{3d}_{c1} \approx 0.0111$ (marked by a cross in Fig. 15) and continues all the way to $\mu = 0$. The two solutions with the largest norm at $\mu = 0$ correspond to stable and unstable steady drop ($SD_1$) solutions, connected via a saddle-node bifurcation at $\mu^{3d}_{sn2} \approx 0.002\,019$ [Fig. 16(a)]. Such solutions are present whenever $L > L^0_{sn1}$. Time simulations at $\mu$ slightly above $\mu^{3d}_{sn2}$ with a stable steady drop as initial condition show that the saddle-node bifurcation is not a sniper bifurcation: the steady drop does not start to slide but instead stretches in the $y$ direction and converges to the stable 2D $SR_1$ state.

The transition from (iia) to (iib) is now clear: with increasing $L$ the saddle-node bifurcation between the branches $SD_2$ and $SD_3$ [at $\mu^{3d}_{sn1}$; cf. case (iia)] moves toward $\mu = 0$. At $L = L^0_{sn2}$ it touches the line $\mu = 0$ and two new solutions appear at $\mu = 0$ corresponding to the $SD_2$ and $SD_3$ branches in Fig. 5. In contrast, the behavior of the sliding solutions remains unclear. The 2D oscillations and stick-slip states (Fig. 7) continue to exist but are now unstable with respect to 3D perturbations, and time simulations result in stick-slip drops. Since this branch does not terminate in a local bifurcation we conjecture that it terminates in a global bifurcation on the (unstable) $SD_2$ branch. The discussion in Sec. IV supports this interpretation as does Ref. [86].

In Fig. 17 we show logarithmic fits to the SSD period $T$, i.e., the time it takes for a drop to slide to the next downstream

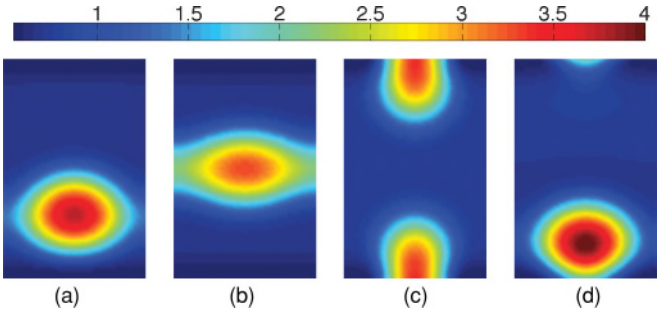


FIG. 16. (Color online) Scenario (iib): Steady states at locations indicated by open squares in Fig. 15 in terms of contours of constant $h(x,y)$. Drops at (a) the saddle node $\mu_{\rm sn2}^{\rm 3d} \approx 0.0020$ on the $SD_1$ branch, and on the $SD_2$ branch at (c) $\mu = 0$ and (d) $\mu = 0.0070$. The modulated ridge $SD_1$ shown in (b) is also at $\mu = 0$.

defect following depinning, as a function of $\mu$ for $L = 26$ (cf. Fig. 15) and $L = 27$ (cf. Fig. 19). The points near the critical parameter value $\mu = a_1 \approx \mu_g^{\rm 3d}$ are given the highest weight. A square-root power law of the type expected near a sniper bifurcation is not compatible with the data, while the logarithmic fit shown in the figure provides strong evidence for depinning via a global bifurcation for both $L = 26$ and $L = 27$. We caution, however, that fits of this type cannot exclude the presence of a fold in the SSD branch prior to depinning ($\mu \to \mu_g^{\rm 3d}$, $T \to \infty$) because of the absence of very high-period simulations. On the other hand, the figure clearly differentiates between the global bifurcations present for $L = 26$ and $L = 27$ and sniper bifurcations present for $L = 27.8$ (cf. Fig. 21 below) and larger $L$, for which a square-root fit works very well.

The logarithmic fits provide information about the leading eigenvalues of the saddle-type equilibria responsible for the presence of the global bifurcation suggested by the fits. We assume that the two leading eigenvalues of the equilibrium at $\mu = a_1$ (i.e., the eigenvalues closest to zero) are real, with one positive eigenvalue $\lambda_u > 0$ and one negative eigenvalue $\lambda_s < 0$. We assume that all the remaining eigenvalues, whether real or complex, are stable with modulus larger than $|\lambda_s|$. Under these circumstances standard theory shows that near $\mu = a_1$, the period follows the asymptotic behavior $T \approx -\frac{1}{\lambda_u}\ln(\mu - a_1)$ provided $\lambda_u + \lambda_s < 0$, and $T \approx \frac{1}{\lambda_s}\ln(\mu - a_1)$ provided $\lambda_u + \lambda_s > 0$. In the former case the periodic orbit is stable near $\mu = a_1$; in the latter it is unstable. However, in both cases the growth of the period is asymptotically monotonic with the distance from $\mu = a_1$.

We have computed the leading eigenvalues along the $SD_2$ and $SD_3$ branches for the two values of $L$. Both branches are of saddle type near the global bifurcation and hence candidates for involvement in the global bifurcation. Figure 18 shows that for (a) $L = 26$ the two leading eigenvalues of $SD_2$ at $\mu = a_1 \approx 0.009\,39$ are $\lambda_u = 0.0140$ and $\lambda_s = -0.003\,96$, while for (b) $L = 27$ the leading unstable eigenvalue at $\mu = a_1 \approx 0.008\,10$ is $\lambda_u = 0.0101$ and the leading stable eigenvalue is complex, with real part $\mathrm{Re}\lambda_s = -0.004\,20$. Thus the theory summarized above applies in the first case only; the complex eigenvalues in the second case suggest an oscillatory approach to the global bifurcation of Shil'nikov type that is not observed. In the first case the fact that $\lambda_u + \lambda_s > 0$ indicates that the appropriate prefactor in the scaling of the asymptotic

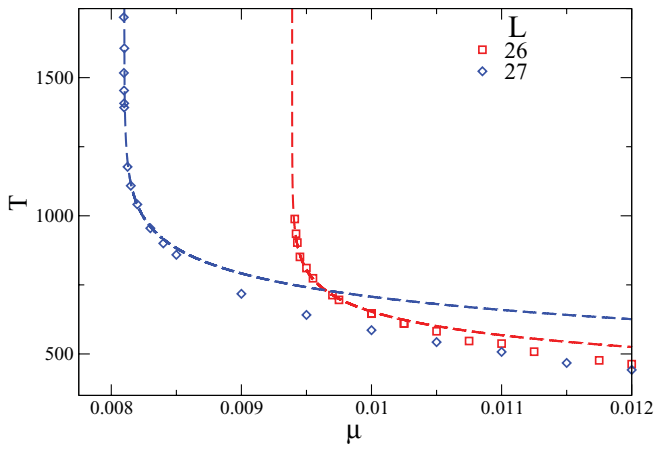


FIG. 17. (Color online) Temporal period $T$ of stick-slipping drop (SSD) solutions as a function of the driving force $\mu$ for $L = 26$ and $L = 27$ (see legend). In each case the first six points were used for a fit of the form $T = -a_0 \ln(\mu - a_1)$ (dashed lines). The fit parameters are $a_0 = 88.3$, $a_1 = 0.009\,39$ for $L = 26$, and $a_0 = 112.85$, $a_1 = 0.008\,10$ for $L = 27$.

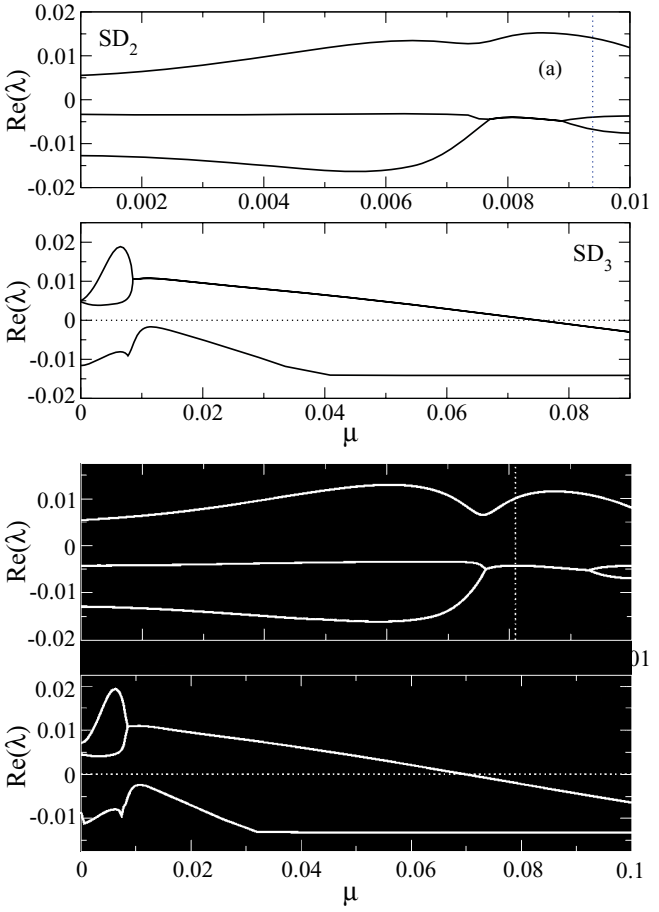


FIG. 18. Real part of the leading eigenvalues of the $SD_2$ and $SD_3$ branches for (a) $L = 26$ (Fig. 15) and (b) $L = 27$ (Fig. 19). The dotted line indicates the approximate location of the global bifurcation, i.e., $\mu = a_1$ (Fig. 17). As $\mu$ increases the $SD_3$ branch stabilizes via a Hopf bifurcation at $\mu_{\rm Hopf}^{\rm 3d} \approx 0.075$ ($L = 26$) and at $\mu_{\rm Hopf}^{\rm 3d} \approx 0.07$ ($L = 27$), respectively.

period is $a_0 = 1/|\lambda_s| \approx 252.5$. This value does not compare well with the fit (a) in Fig. 17. As in the 2D case we surmise that this discrepancy is due to the fact that $\lambda_u + \lambda_s > 0$ implies that if $SD_2$ is responsible for the global bifurcation the nearby periodic orbits will necessarily be *unstable*. Thus the branch of periodic states must in fact overshoot the global bifurcation, and double back, i.e., the branch *must* undergo a saddle-node bifurcation and lose stability prior to the global bifurcation, much as in the 2D case discussed in Fig. 7. However, in contrast to Fig. 7, in the 3D case we have been unable to detect any evidence for a saddle node of the SSD states in this region. Likewise in the second case the fact that $\lambda_u + 2\mathrm{Re}\lambda_s > 0$ implies that all long-period SSD states will also be unstable.

Close to $\mu = \mu_g^{3d}$, but before the asymptotic regime just described sets in, the periodic orbits are, however, stable, and in this case the period should be approximated by $T \approx -\frac{1}{\lambda_u}\ln(\mu - a_1)$, i.e., we expect that in this regime the correct value of $a_0$ is $a_0 \approx 71.4$ ($L = 26$). This result is to be compared with the fit $a_0 = 88.3$ (Fig. 17). Of course, because of the overshoot, the fitted value of $a_1$, $a_1 \approx 0.009\,39$, is smaller than the true value $\mu = \mu_g^{3d}$, and this is so in case (b) as well. Here the fit yields $a_0 \approx 112.85$ ($L = 27$) which again compares well with $\frac{1}{\lambda_u} = 101.3$.

#### 4. Scenario (iiia): $L_{c1}^0 \leqslant L \leqslant L_1$

As $L$ increases beyond $L_{c1}^0$ two related changes occur simultaneously at $\mu = 0$: the 2D $SR_1$ state becomes linearly unstable and the subcritical part of the $SD_1$ branch is no longer present (cf. Fig. 3). As a result when $\mu$ increases the $SR_1$ acquires stability with respect to the Plateau-Rayleigh instability at $\mu_{c2}^{3d} \approx 0.000\,286$ (for $L = 27$) before losing it again at $\mu_{c1}^{3d} \approx 0.010\,778\,3$ (Fig. 10). The resulting bifurcation diagram obtained using continuation together with time-stepping computations is shown in Fig. 19. Selected steady profiles are shown in Fig. 20. Although the linear stability properties of the $SR_1$ state do not change when $L$ increases toward $L_{\max}$, the bifurcation diagram changes its appearance twice owing to codimension two bifurcations that take place at $L = L_1$ and $L = L_2$ (see below). We treat the resulting $L$ regimes in cases (iiia), (iiib), and (iiic), respectively.

The main difference between case (iiia) and the scenario (iib) already discussed is found in the behavior of the unstable part of the $SD_1$ branch. In (iiia) this branch does not extend to $\mu = 0$ but terminates instead on the $SR_1$ branch in a subcritical bifurcation at $\mu_{c2}^{3d}$. With increasing amplitude the unstable part of the $SD_1$ branch turns around in a "true" saddle-node bifurcation at $\mu_{sn2}^{3d} \approx 0.003\,701\,5$ and acquires stability. Time evolution at $\mu$ slightly above the saddle node at $\mu_{sn2}^{3d}$ starting from a stable drop at lower $\mu$ converges to the stable $SR_1$ solution. Examples of profiles on the $SD_1$ branch are shown in Fig. 20. The bifurcation at $\mu_{c1}^{3d}$ also generates subcritical 3D steady states. As in scenario (iib) these extend all the way to $\mu = 0$, albeit with a slightly higher and more pointed maximum norm. The norm at small $\mu$ is also larger and is now comparable to the amplitude of the $SR_1$ states. For $\mu > \mu_{c1}^{3d}$ time evolution results in a family of stick-slip drops.

#### 5. Scenario (iiib): $L_1 \leqslant L \leqslant L_2$

At $L = L_1 = 27.59$ a codimension-2 bifurcation takes place and the bifurcation diagram changes from Fig. 19 to that

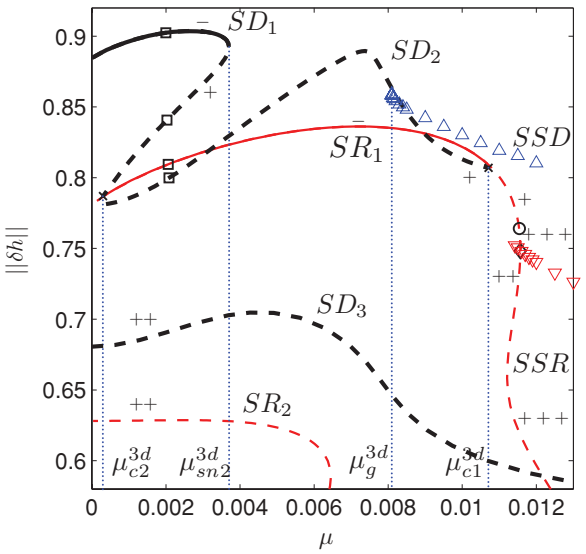


FIG. 19. (Color online) Scenario (iiia): Bifurcation diagram for steady ridges (SR, thin red lines) and steady drops (SD, black lines) on a substrate with hydrophobic line defects (wettability contrast $\epsilon = 0.3$) and spanwise system size $L = 27$ showing the $L^2$ norm $||\delta h||$ of steady solutions as a function of the driving force $\mu$. Solid (dashed) lines denote stable (unstable) solutions. Downward (upward) pointing triangles indicate SSR (SSD) solutions. Solution profiles at locations indicated by open squares are shown in Fig. 20. The remaining parameters are the same as in Fig. 3.

in Fig. 21(a). The figure shows that no qualitative change in behavior occurs at zero or small $\mu$. The $SR_1$ branch is unstable at $\mu = 0$ and stabilizes at $\mu_{c2}^{3d} \approx 0.001\,079\,8$ (for $L = 27.8$). This bifurcation continues to be subcritical and produces a branch $SD_1$ of unstable 3D states. The $SD_1$ states annihilate in a true saddle-node bifurcation at $\mu_{sn2}^{3d} \approx 0.005\,816\,1$. However, the 3D solutions that emerge subcritically at $\mu_{c1}^{3d} \approx 0.010\,478\,9$ and extend to $\mu = 0$ undergo a major change near maximum norm. At $L = L_1$ a cusp appears and for $L > L_1$ the branch develops a loop, with two additional saddle-node bifurcations, at $\mu_{sn3}^{3d} \approx 0.006\,987\,2$ and $\mu_{sniper}^{3d} = \mu_{sn4}^{3d} \approx 0.007\,234\,2$ (for $L = 27.8$), as visible in the zoom in Fig. 21(b). At the same time the branch acquires a linearly stable segment that extends between the two saddle-node bifurcations. A sample stable solution is shown in Fig. 22(b). Moreover, while the left-hand

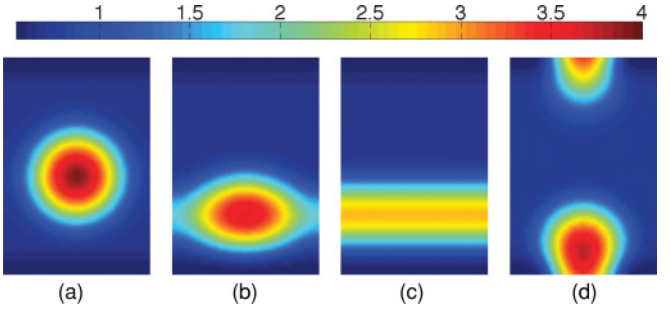


FIG. 20. (Color online) Scenario (iiia): Steady states at locations indicated by open squares in Fig. 19 in terms of contours of constant $h(x,y)$, ordered by decreasing norm. (a) $\mu = 0.001\,99$, (b) $\mu = 0.002\,03$, (c) $\mu = 0.001\,88$ and (d) $\mu = 0.002\,08$.

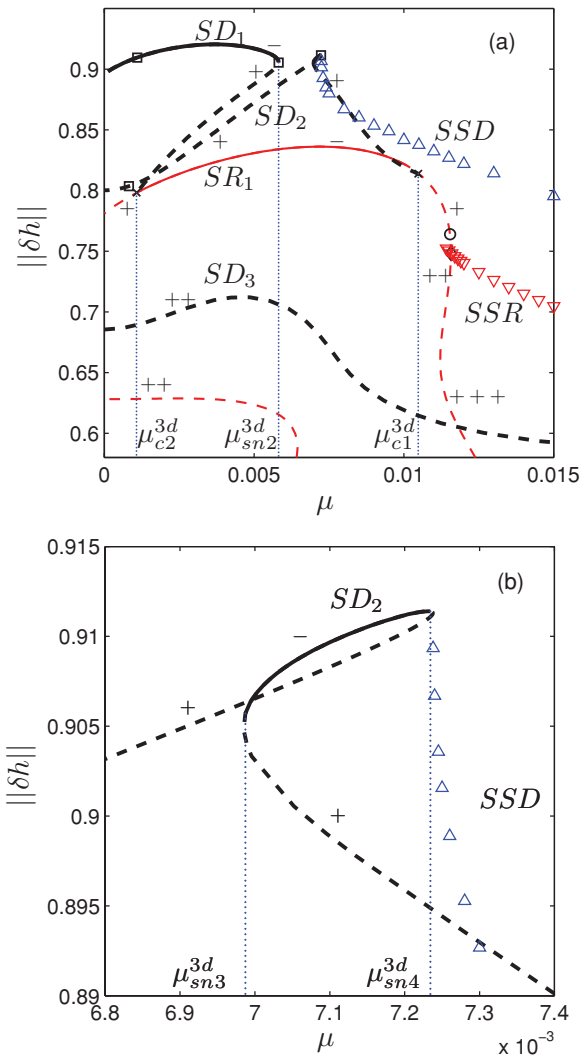


FIG. 21. (Color online) Scenario (iiib): (a) Bifurcation diagram for steady ridges (SR, thin red lines), and steady drops (SD, black lines) pinned by a hydrophobic line defect of strength $\epsilon = 0.3$ for $L = 27.8$ showing the $L^2$ norm $||\delta h||$ of steady solutions as a function of the driving force $\mu$. Solid (dashed) lines denote stable (unstable) solutions. (b) shows a zoom of the cusplike feature on the $SD_2$ branch. The $SD_3$ branch becomes stable at $\mu = 0.064$ (not shown). Downward (upward) pointing triangles indicate SSR (SSD) solutions. Solution profiles at locations indicated by open squares are shown in Fig. 22. The remaining parameters are the same as in Fig. 3.

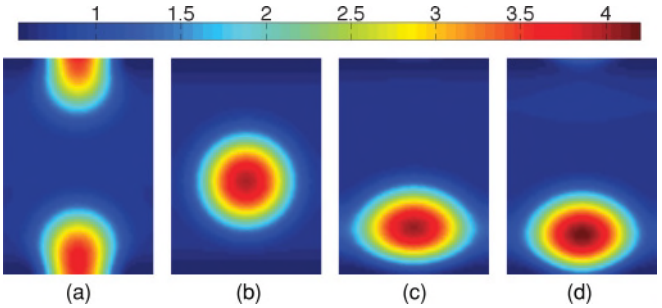


FIG. 22. (Color online) Scenario (iiib): Steady states at locations indicated by open squares in Fig. 21 in terms of contours of constant $h(x,y)$. (a) $\mu = 0.000\,82$ on the unstable part of the drop branch $SD_1$, (b) on the stable part of the drop branch $SD_1$ at $\mu = 0.001\,10$, (c) at the saddle-node $\mu^{3d}_{sn2} = 0.005\,82$ on $SD_1$, and (d) at the sniper bifurcation at $\mu^{3d}_{sn4} = 0.007\,24$ on $SD_2$.

saddle node at $\mu^{3d}_{sn3}$ is a true saddle node, that at $\mu^{3d}_{sniper} = \mu^{3d}_{sn4}$ now corresponds to a sniper bifurcation, with a branch of stick-slip drops emerging from $\mu^{3D}_{sniper}$.

With increasing $L$ the topology of the diagram remains unchanged until a second critical value, $L = L_2$, as discussed next.

### 6. Scenario (iiic): $L_2 \leqslant L \leqslant L_{max}$

When $L$ is increased beyond $L_2 = 27.87$ another codimension-2 bifurcation takes place and the bifurcation diagram changes from Fig. 21(a) to that in Fig. 23. Once again the branches at $\mu = 0$ and their stability properties remain unchanged, as do the properties of the $SR_1$ states. However, the nonlinear behavior at finite $\mu$ changes dramatically, with the 3D branches in Fig. 21(a) reconnecting in a new way. This reconnection occurs as a result of the fusion/annihilation of the saddle-node at $\mu^{3d}_{sn2}$ on the $SD_1$ branch and the newly created saddle node at $\mu^{3d}_{sn3}$ on the branch of 3D states $SD_2$ via a "necking" bifurcation. As a result the branches reorder into a simpler bifurcation pattern [Fig. 23(a)], with the stable part of $SD_1$ connecting to the stable part of $SD_2$ and the unstable part of $SD_1$ connecting to the right unstable part of $SD_2$. Thus $\mu^{3d}_{sniper}$ remains at $\mu^{3d}_{sn4}$, with $\mu^{3d}_{sn4} \approx 0.006\,905\,5$ in Fig. 23(a). Thus, as a result of the various transitions occurring with increasing $L$, the depinning transition has shifted from the 2D $SR_1$ states [39] to the 3D $SD_1$ states [41], i.e., the behavior expected of large drops in large domains.

Figure 23(b) shows the eigenvalues along the stable and unstable parts of the $SD_1$ branch and reveals that the leading eigenvalue of the stable drop solution is complex close to the saddle node at $\mu^{3d}_{sniper}$. In this regime the stable $SD_1$ states relax in an oscillatory fashion when perturbed. In contrast, the leading unstable eigenvalue along the unstable $SD_1$ branch is real, implying monotonic growth. This eigenvalue is created by a collision of the complex eigenvalues on the negative real axis prior to the saddle-node bifurcation creating a pair of real eigenvalues, one of which crosses into the positive half plane at $\mu^{3D}_{sniper}$.

At the same time the branch of unstable 3D states that emerges at $\mu^{3d}_{c2} \approx 0.002\,578\,2$ continues toward and ends at $\mu^{3d}_{c1} \approx 0.010\,065$. As $L$ is increased further, $\mu^{3d}_{c1}$ and $\mu^{3d}_{c2}$ approach each other until they annihilate at $L_{max}$ (Fig. 10). Consequently the branch $SD_2$ of unstable 3D states becomes shorter and shorter, along with the interval of stable $SR_1$ states, and when it vanishes so does the $SR_1$ stability interval. However, for the parameter values of Fig. 23(a) we find coexistence between stable $SR_1$ states and either stable $SD_1$ states or, beyond the sniper bifurcation at $\mu^{3d}_{sniper} = \mu^{3d}_{sn4}$, (numerically stable) stick-slip drop motion.

### 7. Scenario (iv): $L_{max} \leqslant L$

As just indicated, for $L > L_{max}$ the spanwise-invariant ridge $SR_1$ is linearly unstable for all $\mu$ with a real positive leading eigenvalue [Fig. 10] and the unstable $SD_2$ branch is absent. Moreover, the 3D drop states $SD_1$ now correspond to

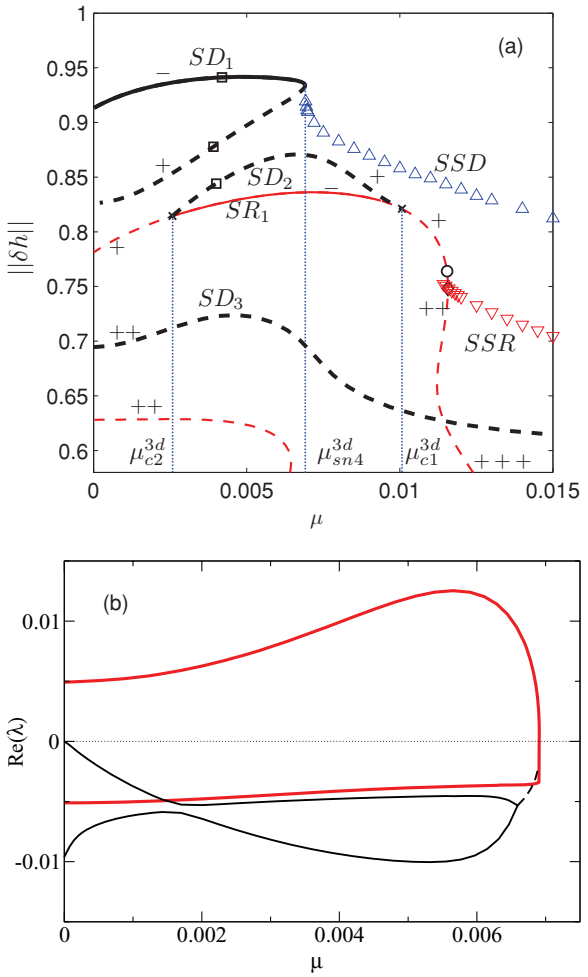


FIG. 23. (Color online) Scenario (iiic): Bifurcation diagram for steady ridges (SR, thin red lines), and steady drops (SD, black lines) on a substrate with hydrophobic line defects (wettability contrast $\epsilon = 0.3$) and spanwise system size $L = 29$ showing the $L^2$ norm $||\delta h||$ of steady solutions as a function of the driving force $\mu$. Solid (dashed) lines denote stable (unstable) solutions. Downward (upward) pointing triangles indicate SSR (SSD) solutions. Solution profiles at locations indicated by open squares are shown in Fig. 24. The remaining parameters are as in Fig. 3. The $SD_3$ branch becomes stable at $\mu = 0.062$ (off scale). (b) Real part of the leading eigenvalues for the stable (thin black line) and unstable part (heavy red line) of $SD_1$ drop branch. The black dashed line corresponds to a complex eigenvalue.

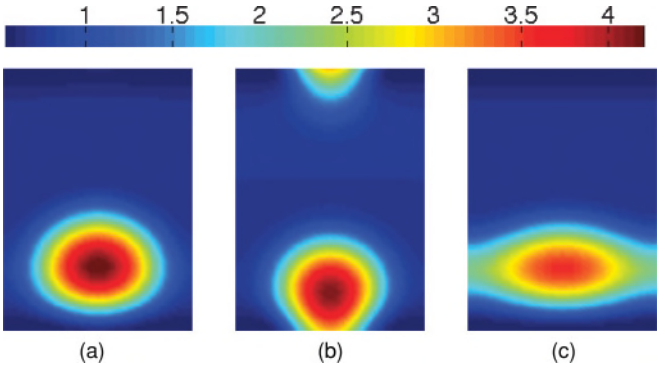


FIG. 24. (Color online) Scenario (iiic): Steady states at locations indicated by open squares in Fig. 23 in terms of contours of constant $h(x,y)$, ordered by decreasing norm. (a) $\mu = 0.004\,19$, (b) $\mu = 0.003\,91$, and (c) $\mu = 0.004\,01$. The remaining parameters are as in Fig. 3.

the drops studied in [41], i.e., in large domains. In Fig. 25 the sniper bifurcation occurs at $\mu^{3d}_{sn4} \approx 0.0069$ and the emerging SSD branch approaches the $SD_3$ branch with increasing $\mu$, connecting to it in a Hopf bifurcation at $\mu^{3d}_{Hopf} \approx 0.051$. Since at large $\mu$ the $SD_3$ states resemble modulated rivulets [cf. Fig. 14(c)] close to the Hopf bifurcation the SSD states correspond to surface waves on a steady rivulet.

### D. Stability in the $(L,\mu)$ plane

The bifurcation analysis in the preceding sections has identified several types of stable steady (ridge, drop, and rivulet) and time-periodic (stick-slipping ridge and stick-slipping drop) states. Figure 26 displays the stability regions of these states in the $(L,\mu)$ parameter plane. Most of the boundaries of these regions are computed by numerically tracking the bifurcations that lead to loss of stability. For example, since the drop state loses stability via a saddle-node or a sniper bifurcation, one of the stability boundaries requires the tracking of a zero eigenvalue of the linear problem obtained by linearizing Eq. (1) about the drop state. This is accomplished using a steady-state continuation algorithm similar to that described in [54]. Likewise, since the rivulet state is stabilized via a Hopf bifurcation, numerical tracking of the Hopf bifurcation yields the stability boundary of the rivulet state.

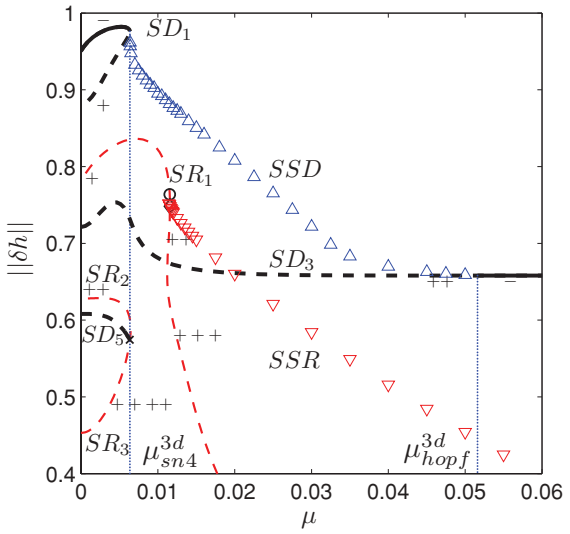


FIG. 25. (Color online) Scenario (iv): Bifurcation diagram for steady ridges (SR, thin red lines), and steady drops (SD, black lines) on a substrate with hydrophobic line defects (wettability contrast $\epsilon = 0.3$) and spanwise system size $L = 32$ showing the $L^2$ norm $||\delta h||$ of steady solutions as a function of the driving force $\mu$. Solid (dashed) lines denote stable (unstable) solutions. Downward (upward) pointing triangles indicate SSR (SSD) solutions. The remaining parameters are as in Fig. 3. The $SD_3$ branch becomes stable at $\mu^{3d}_{Hopf} \approx 0.051$.

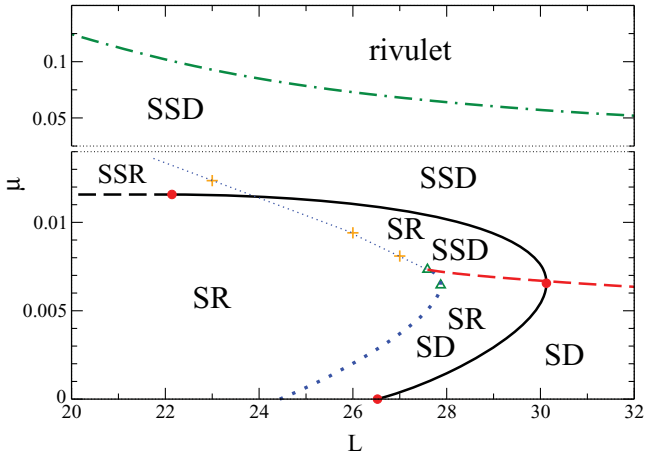


FIG. 26. (Color online) Stability diagram for steady (SR) and stick-slipping ridge (SSR), steady (SD) and stick-slipping drop (SSD), and rivulet states on a heterogeneous incline showing the region of stability in the $(L,\mu)$ plane for $\epsilon = 0.3$, $\bar{h} = 1.2$, and $L_x = 40$. Black solid (dashed) lines indicate the transversal (sniper) instability of the steady ridges as in Fig. 10. The thick dotted blue (dashed red) lines are the loci of saddle-node (sniper) bifurcations of the drop states. The thin dotted blue line indicates the hypothetical border of the region of stable stick-slipping drops (the three "+" symbols result from our calculations). Finally, the dot-dashed green line indicates the loci of the Hopf bifurcation where the steady 3D rivulets become stable when $\mu$ increases.

The region of stable steady ridge solutions is discussed in Sec. II B 2. Note that it has some overlap with the region of stable steady drop states. This indicates bistability and implies that, in the intersection region, the observed state depends on initial conditions. The region of stable steady drop solutions is delimited by two curves which end in a cusp (upper green triangle) corresponding to the codimension-2 bifurcation at $(L_1,\mu_1)$ (see Sec. III C 5). The leftmost boundary of the SD region (thick blue dotted line in Fig. 26) starts from the point $(L^0_{\rm sn1},\mu = 0)$ and terminates at the cusp. The turning point at $(L_2,\mu_2)$ (lower green triangle) corresponds to the codimension-2 bifurcation identified in Sec. III C 6. This dotted boundary is the locus of true saddle nodes, i.e., a drop destabilized at this boundary does not start to slide but instead stretches and converges to a stable ridge solution (see Sec. III C 3). In contrast, the upper boundary of the SD region (red dashed line in Fig. 26) corresponds to sniper bifurcations, and loss of stability along this boundary results in periodic stick-slip motion. This scenario occurs even if the sniper boundary intersects the stable ridge region. The resulting stick-slip motion is stable as shown by time integration, and corroborated in the next section.

We are not, however, able to compute in detail the region of stable stick-slip motions for $L < L_1$ since this requires the knowledge of the loci of global homoclinic bifurcations, a difficult task for a problem of this complexity. Instead we indicate the hypothetical boundary of the region of stick-slip drop motion by a thin blue dotted line, guided by the orange crosses. These indicate the "end" of the branch of stick-slipping drops as found in time simulations for selected $L$. Note, however, that the transition at the thin blue dotted line involves some hysteresis, at least outside the steady-ridge region, where simulations indicate some overlap between regions of stable stick-slip ridges and stick-slip drops. The extent of this hysteresis region remains unknown.

At large $\mu$ one encounters a region of stable rivulets. This region does not intersect the other stability regions (note the broken $y$ axis in Fig. 26). The critical driving $\mu_{\rm Hopf}(L)$ corresponding to the stability boundary increases rapidly with decreasing $L$.

## IV. INTERPRETATION

In this section we provide a bifurcation theory interpretation of the transition sequences described in the preceding section. We focus on the transitions observed for $L = 29$, $L = 27$, and $L = 23$ as the forcing $\mu$ varies. These transitions involve first and foremost the saddle-node bifurcation(s) on the steady-ridge branch $\mathrm{SR}_1$ (hereafter SR). In addition to this bifurcation we have identified two nearby bifurcations, a Hopf bifurcation that leads to time-periodic oscillations of the ridge state, and a steady-state bifurcation that breaks the invariance of the ridge state in the spanwise direction, leading to steady droplike states (SDs). In addition, we have found two time-dependent solution types, sliding stick-slip ridges (SSRs) and sliding stick-slip droplike states (SSDs).

Our computations reveal that both the Hopf and symmetry-breaking steady-state bifurcations occur close to the upper saddle-node bifurcation, suggesting that the different bifurcation scenarios may be understood by examining the interaction between these three bifurcations, i.e., a codimension-3 bifurcation. The inclusion of the nearby lower saddle-node bifurcation would require a study of codimension 4 in which a hysteresis bifurcation interacts with both a Hopf bifurcation and a steady-state bifurcation. Bifurcations of this complexity have not been studied in full detail, e,g., [87]. Moreover, the standard approach using normal form theory describes solutions in $\mathrm{R}^3$, the dimension of the (extended) center manifold for a mode interaction of this type. This reduction in dimension is a consequence of normal form symmetry, which decouples the phase associated with the Hopf bifurcation from its amplitude.

The three-dimensional phase space $\mathrm{R}^3$ allows of course complex (chaotic) dynamics [88,89] but is unable to accommodate the sniper bifurcations that lead to sliding states. For this purpose the problem must be posed in $\mathrm{R}^2\times\mathrm{S}^1$, i.e., with periodic boundary conditions inherited from the periodicity of the problem in the downstream direction. This type of phase space allows two types of periodic orbits, those that oscillate about an equilibrium (librations) and those for which the periodic variable increases by $2\pi$ each period (rotations). These solution types can be visualized in terms of the standard pendulum, with librations corresponding to standard pendulum oscillations and rotations corresponding to a whirling pendulum.

Although no rigorous normal form theory exists for this case (the rotations rely on global properties of the phase space) model problems with the required properties are readily constructed (e.g., [89]). The most relevant such model was

constructed by Krauskopf and Oldeman [90], who investigated the properties of the following system of equations:

$$\dot{\rho} = \nu_1 \rho - a\rho \sin\varphi - \rho^3, \tag{6}$$

$$\dot{\varphi} = \nu_2 + s\rho^2 + 2\cos\varphi + c\rho^4. \tag{7}$$

The model can be viewed in two ways, as an interaction between a saddle-node bifurcation in a periodic orbit (sniper) and a Hopf bifurcation, or as an interaction between a sniper and a symmetry-breaking pitchfork bifurcation. In the former the variable $\rho > 0$ corresponds to the amplitude of the periodic oscillations (the temporal phase decoupling in "normal form") while in the latter $\rho$ corresponds to the amplitude of the state created in the symmetry-breaking pitchfork bifurcation. Both interpretations rely on the symmetry $\rho \to -\rho$ of the model and are relevant to the depinning problem.

We examine first the depinning problem in which the steady ridge state does not undergo a Hopf bifurcation. In this case the system (6) and (7) describes the dynamics near the codimension-2 point $(\mu_{CT}, L_{CT})$ at which the symmetry-breaking pitchfork of the SR state coincides with the saddle-node bifurcation at $\mu = \mu_{sn1}^{2d}$. Thus $(\nu_1, \nu_2)$ represent linear combinations of $\mu - \mu_{CT}$ and $L - L_{CT}$. In this case the variable $\rho > 0$ represents the amplitude of the translation-invariance-breaking instability creating the SD state, the spanwise phase of the mode having decoupled because of translation invariance of the SR state in the spanwise direction. The variable $\varphi$ plays the role of the downstream coordinate. Thus equilibria with $\rho = 0$ represent SR states while periodic solutions with $\rho = 0$ correspond to sliding ridges. Equilibria with $\rho \neq 0$ correspond to stationary drops while periodic solutions with $\rho \neq 0$ are of two types, oscillations about an SD state (librations) and sliding drops (rotations, SSDs).

In Fig. 27 we reproduce Fig. 7 of [90]. The central part of the figure shows the $(\nu_1, \nu_2)$ parameter plane; in the depinning problem these parameters correspond to different combinations of the parameters $\mu$ and $L$. The $(\nu_1, \nu_2)$ plane is split into a number of distinct regions, labeled by integers, with distinct phase space dynamics. The phase portraits characteristic of each region are shown along the periphery of the diagram, with the variable $\rho$ shown horizontally and $\varphi$ vertically. The lines $S_0$ in the $(\nu_1, \nu_2)$ plane correspond to saddle-node bifurcations with $\rho = 0$, i.e., to snipers on the SR state, and are located at $\nu_2 = \pm 2$. The ellipse $P$ corresponds to pitchfork bifurcations of equilibria with $\rho = 0$, i.e., to steady bifurcations from SR to SD states. The line $S$ corresponds to saddle-nodes of SD states (the point labeled BT is a Takens-Bogdanov point with a double zero eigenvalue). Finally the curves labeled $Z$ indicate the transition from SSR states to SSD states, i.e., transitions from a rotation with $\rho = 0$ to a rotation with $\rho > 0$. The curves $S_0$, $P$, and $Z$ meet at points labeled $B^{\pm}$. The additional lines all correspond to different types of global bifurcations detailed in [90].

We are now in a position to interpret the dynamics observed in this paper in terms of the truncated normal form (6), (7). Specifically, the pinning transition observed as $\mu$ decreases, for example, for $L = 32$ (Fig. 25), corresponds to traversing from region 13 (unstable SSR, stable SSD) to region 12 (a pair of unstable SRs and a stable SSD) to region 3 (a pair of unstable SRs and a pair of SD, one stable, one unstable). The transition from region 12 to region 3 is thus a standard sniper, except that the equilibria created in the transition are of SD type.

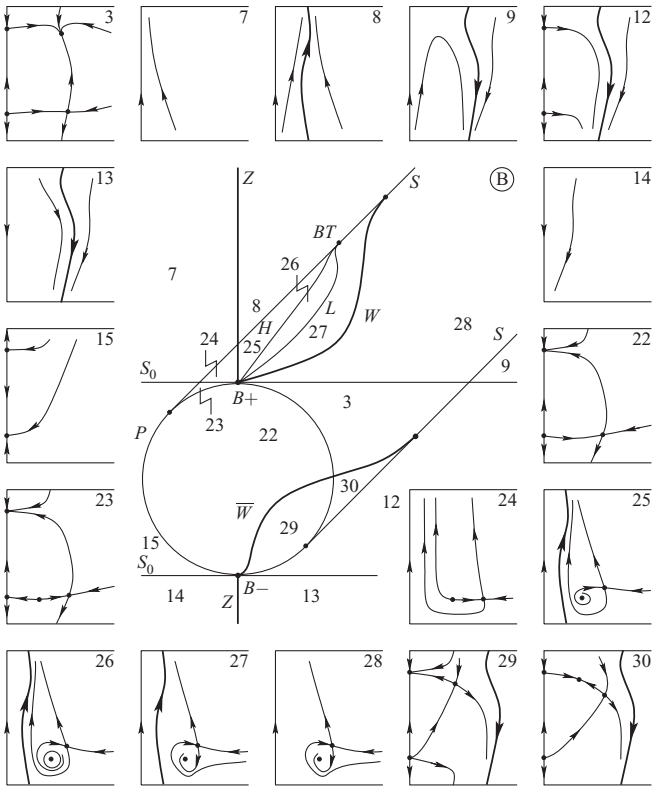


FIG. 27. The $(\nu_1, \nu_2)$ parameter plane for the system (6), (7) with $a = 0.5$, $c = 0$, $s = -1$ (case B of [90]) showing the codimension-1 lines $S_0$, $P$, $S$, and $Z$ discussed in the text. The Takens-Bogdanov point is labeled BT. The remaining curves correspond to global bifurcations. The phase portraits around the periphery show solutions characteristic of each of the numbered regions in the $(\rho, \phi)$ plane. Reproduced with permission from [90].

When $L = 27$ the depinning transition summarized in Fig. 19 is consistent with a slightly different cut through the $(\nu_1, \nu_2)$ plane. This time we pass from region 13 to region 12 followed by region 29 (a pair of SR states, one of which is stable and the other unstable, an unstable SD state created in a subcritical pitchfork bifurcation, and a stable SSD state) and region 22 (a pair of SR states, one of which is stable and the other unstable, and an unstable SD state). Note that the disappearance of the SSD state is the result of a standard homoclinic bifurcation, a collision of a periodic orbit with a single saddle-type equilibrium, here an SD state, as suggested by Fig. 17. Reference [90] shows that these transitions are robust for $a > 0$, $c = 0$, $s < 0$ [Eqs. (6) and (7)] and represent the simplest transitions from among the possibilities shown in Fig. 27 and related figures valid in other parameter regimes.

We next consider the transition observed for $L = 23$ (Fig. 13). We have not been able to interpret this transition within the two-dimensional system (6), (7). The main obstacle for this interpretation is the coexistence of a stable SSR state with a pair of *unstable* SR states, a possibility that is not permitted within Eqs. (6) and (7) when $\rho = 0$. Indeed, Fig. 13 indicates that in this case the SR state depins via a

Hopf bifurcation, a possibility that can only be captured by a higher-codimension normal form. On the other hand the observed transition from SSD to SSR resembles that along the line $Z$ between regions 13 and 14 in Fig. 27, except for the fact that in Fig. 13(b) this transition is apparently subcritical.

Since the normal form (6), (7) was constructed to describe the interaction between a Hopf and a sniper bifurcation, we can also examine its applicability in the two-dimensional depinning problem, i.e., for spanwise-invariant ridge states. Figure 7(b) shows the transition observed when three-dimensional instabilities are suppressed. The same transition forms part of the behavior in Fig. 13 despite the presence of 3D instability. To use Fig. 27 we need to recall that fixed points of Eqs. (6) and (7) with $\rho > 0$ now correspond to constant amplitude *oscillations* (OR) about an SR state. Thus the standard sniper bifurcation corresponds to a transition from region 14 to region 15. But when a Hopf bifurcation occurs on SR prior to the saddle-node at $\mu_{\rm sn1}^{\rm 2d}$ the sniper bifurcation is replaced by a new depinning transition as described in Sec. III B. The SSR state now involves oscillations about the SR state and so is represented in Fig. 27 by a rotation at finite $\rho$. As seen from the behavior of the period in the inset in Fig. 7(b) this state disappears in a global bifurcation. We expect that this global bifurcation involves the unstable oscillations (librations) created at $\mu_{\rm hopf}^{\rm 2d}$. In Fig. 27 this sequence of transitions is described by traversing from region 13 (stable SSR state with superposed oscillations) into region 12 (a pair of unstable SR states together with a stable SSR state with superposed oscillations) and then into region 29 (a pair of SR states, one of which is stable and the other unstable, together with an unstable libration and a stable SSR state with superposed oscillations). The pinning transition takes place on crossing from region 29 into region 22 (a pair of SR states, one of which is stable and the other unstable, together with an unstable libration) and so involves the formation of a homoclinic connection to a periodic orbit. Note that in this scenario the SSR state in Fig. 7(b) is a *two-frequency* state while the libration that is left has a single *finite* frequency.

Our calculations indicate that the SSR state is in fact a single-frequency state. As a result we favor a different explanation for the behavior shown in Fig. 7(b). This behavior involves a global bifurcation between a single-frequency rotation (SSR) and a single-frequency oscillation (OR) about an SR state, a transition that is organized by a Takens-Bogdanov bifurcation with periodic reinjection. At the Taken-Bogdanov point the Hopf bifurcation coincides with the saddle node and the Hopf frequency *vanishes*. Consequently the normal form (6), (7) no longer applies. The Takens-Bogdanov point can be identified by shifting the parameter $\epsilon$ appropriately and recomputing the leading eigenvalues along the SR branch to find the point $(\mu_{\rm TB},\epsilon_{\rm TB})$ at which the zero eigenvalue has double multiplicity. Although we have not performed such a calculation we expect this point to lie close to our chosen parameter values, implying that this bifurcation is likely relevant to the observed dynamics. The normal form for this bifurcation is also two dimensional, and we conjecture that in the presence of reinjection it exhibits the necessary gluing bifurcation. Similar bifurcations are known to occur in spontaneous parity breaking in inhomogeneous systems [91]. However, a study of this problem along the lines of [90] is beyond the scope of this paper.

The virtue of relating our results to something like normal form analysis is that the theory is able to identify "all" types of dynamical behavior that may be present in the vicinity of the origin in the $(\nu_1,\nu_2)$ plane [respectively, $(\mu-\mu_{\rm TB},\epsilon-\epsilon_{\rm TB})$], thereby indicating the *possible* dynamics that may be present in the depinning problem for other parameter values. On the other hand the restriction to a low-dimensional center manifold precludes the presence of complex dynamics. Such behavior is typically associated with the presence of global bifurcations such as those taking place along the curves $L$, $W$, and $\overline{W}$ in Fig. 27. In addition, the theory cannot account for bifurcations that occur "far" from the codimension-2 point. Thus one does not expect to be able to explain all aspects of the computed bifurcation diagrams using low-codimension normal form theory, and this is indeed the case.

## V. CONCLUSIONS

In this paper we have studied the process of depinning of driven liquid drops and ridges on heterogeneous substrates and related transitions between drop and ridge states. In the absence of driving, e.g., on a horizontal substrate, the latter transition is related to the Plateau-Rayleigh instability of a liquid ridge. To explore the three-dimensional dynamics in the presence of driving, we have formulated the depinning process as a bifurcation problem, and focused on a generic problem of this type.

We adopted a simple model problem in which the spatial heterogeneity corresponds to a modulation of the short-range polar contribution to the disjoining pressure and takes the form of parallel hydrophobic stripes with a well-defined spatial period. The stripes are oriented transverse to the driving direction, and may block the passage of ridges and drops, producing strongly asymmetric ridges prior to depinning. In general, pinning might arise from spatially varying wetting properties as here, or from heterogeneous topography, temperature, or electric fields. Possible driving forces include gravitational or centrifugal forces, and/or gradients of wettability, temperature, or electric fields. In the present work we have used gravity as an example, i.e., we have studied drops and ridges on an incline. As a result our approach is limited to drops not much thicker than the wetting layer assumed to be present in our formulation.

The two-dimensional version of this problem was formulated and studied in Ref. [39], where two possible depinning mechanisms were identified: depinning via a sniper bifurcation and depinning via a Hopf bifurcation followed by a global bifurcation that is required for translation of the ridge from one defect to the next. In the present paper we have been interested in like behavior for fully three-dimensional states that we variously refer to as modulated ridges or drops depending on their appearance. Preliminary work on the 3D problem [41] using the numerical procedure described in [54] indicated that for relatively large drops the 3D problem behaves qualitatively in the same way as the 2D problem, but the detailed depinning mechanism was not studied owing to the long time scales involved in the transition region. In this paper

we have therefore focused on the details of the depinning transition in the 3D case.

In three dimensions a transverse liquid ridge has additional avenues open to it since the whole ridge no longer needs to depin simultaneously but can instead send out protruberances through which the fluid flows over the heterogeneity. In this paper we have identified seven distinct regimes depending on the spanwise spatial period $L$ of the computational domain. This spanwise length, if sufficiently small, can suppress vestiges of the Plateau-Rayleigh instability that leads to spanwise modulation of a ridge even on a horizontal substrate. However, on an inclined substrate the choice of $L$ may not only allow a 3D instability to proceed but also determine the volume of liquid that must flow across the heterogeneity and hence the flux of liquid through the rivulets that form as a result of depinning. Thus when $L$ is large three-dimensional instabilities are always present and the depinning of a ridge is preceded by an instability of the 2D ridge that forms 3D droplike states that remain pinned to the heterogeneity, with a further increase in the driving required before depinning takes place.

Our results show that the bifurcation from 2D ridges to 3D droplike states is subcritical, at least for the parameter values we use. As a result the 3D states are initially unstable, although with increasing amplitude the 3D states turn around toward larger values of $\mu$ and may acquire stability once they resemble steady rivulets. However, once the 2D ridges near the 2D sniper are unstable to 3D states, the 2D depinning mechanism no longer leads to stable stick-slip motion of the ridges, and instead we find a stable 3D version, which we call stick-slip drops. Our numerics suggest that in both the 2D and 3D cases the SSR and SSD states terminate in global bifurcations involving equilibria of saddle type. However, the theory of such bifurcations shows that the periodic orbits involved in the global bifurcations are unstable, and indeed our computations in the 2D case provide some evidence of a saddle-node bifurcation in the neighborhood of the putative global bifurcation at which the stable SSR states lose stability. Unfortunately we are unable to follow unstable time-periodic states such as the SSR and SSD states to confirm the presence of such global bifurcations.

We were able, however, to interpret the transitions we observed using a two-dimensional model system analyzed by Krauskopf and Oldeman [90]. This system models the dynamics arising from the interaction of a sniper and a pitchfork, and its analysis reveals the great wealth of behavior available to systems of this type. We expect that transitions present for other values of our parameters can likewise be interpreted in terms of this model system. Model systems such as Eqs. (6) and (7) suffer from a drawback, however, in that the dynamics is necessarily two dimensional and hence no chaos is present in the model. A three-dimensional extension of the model [92] does exhibit chaotic dynamics associated with the plethora of global bifurcations revealed in [90] and offers a glimpse into the potential behavior associated with the (formally infinite-dimensional) depinning problem. However, our simulations have provided no conclusive evidence for chaotic dynamics. In some regimes we have also found a Hopf bifurcation in the 2D depinning problem, usually very close to both the saddle node of the ridge states and the 3D instability, suggesting that the full dynamics of the system can be captured by examining the interaction of the Takens-Bogdanov bifurcation with the pitchfork leading to 3D states [93], with reinjection as in [90].

In the parameter regime where the long-wave approximation applies the problem studied here, viz., film flow and drop motion on a heterogeneous substrate with a well-defined spatial period of the wettability, is closely related to the corresponding flow on the outside or inside of a rotating horizontal cylinder [52]. In particular, the depinning dynamics of a two-dimensional drop of partially wetting liquid on the surface of a rotating cylinder has a close counterpart in the depinning dynamics via a sniper bifurcation described here for two-dimensional drops on heterogeneous substrates [39,52]. Further exploration of the analogy between these two systems may therefore be fruitful. In particular, it may be possible to relate the three-dimensional structures and transitions described in the present paper to flows on rotating cylinders. For instance, the transition from stick-slip drops to spatially modulated rivulets via a Hopf bifurcation (Fig. 25) would correspond to a transition from drops rotating with the cylinder (a state that has apparently not been described in the literature on film flow on the outside of a cylinder) to azimuthal rings [94].

Experiments on pattern formation in flows of thick films on the inner surface of a rotating cylinder report a variety of different structures and transitions that resemble some of our results [95,96]. These include, for instance, stationary straight and wavy fronts (similar to our steady spanwise-invariant ridge and spanwise-modulated ridge states). The latter are called “shark teeth” in [96]. At higher rotation velocities the stationary wavy fronts decay into drops that are “dragged up the receding wall” [95], a transition corresponding to what we describe here as a 3D depinning transition. Stationary localized bumps, i.e., pinned drops, may also be present [95].

## ACKNOWLEDGMENTS

We acknowledge support by the European Union via the FP7 Marie Curie scheme [Grant No. PITN-GA-2008-214919 (MULTIFLOW)], the Deutsche Forschungsgemeinschaft under SFB 486 Project No. B13, and by the National Science Foundation under Grant No. DMS-0908102.

[1] E. B. Dussan, Annu. Rev. Fluid Mech. **11**, 371 (1979).
[2] P.-G. de Gennes, Rev. Mod. Phys. **57**, 827 (1985).
[3] D. Quéré, M. J. Azzopardi, and L. Delattre, Langmuir **14**, 2213 (1998).
[4] P. Brunet, J. Eggers, and R. D. Deegan, Phys. Rev. Lett. **99**, 144501 (2007).
[5] U. Thiele, M. G. Velarde, K. Neuffer, M. Bestehorn, and Y. Pomeau, Phys. Rev. E **64**, 061601 (2001).
[6] J. Eggers, Phys. Rev. E **72**, 061605 (2005).
[7] J. Eggers, Phys. Fluids **17**, 082106 (2005).
[8] L. M. Pismen and U. Thiele, Phys. Fluids **18**, 042104 (2006).

[9] K. John and U. Thiele, Phys. Rev. Lett. **104**, 107801 (2010).
[10] L. W. Schwartz and R. R. Eley, J. Colloid Interface Sci. **202**, 173 (1998).
[11] J. F. Joanny and P.-G. de Gennes, J. Chem. Phys. **81**, 552 (1984).
[12] G. D. Nadkarni and S. Garoff, Langmuir **10**, 1618 (1994).
[13] A. Marmur, Colloids Surf. A **116**, 55 (1996).
[14] P. Collet, J. De Coninck, F. Dunlop, and A. Regnard, Phys. Rev. Lett. **79**, 3704 (1997).
[15] L. W. Schwartz and S. Garoff, Langmuir **1**, 219 (1985).
[16] J. F. Joanny and M. O. Robbins, J. Chem. Phys. **92**, 3206 (1990).
[17] E. Schäffer and P. Z. Wong, Phys. Rev. E **61**, 5257 (2000).
[18] P. Roura and J. Fort, Phys. Rev. E **64**, 011601 (2001).
[19] L. Leger and J. F. Joanny, Rep. Prog. Phys. **55**, 431 (1992).
[20] M. O. Robbins and J. F. Joanny, Europhys. Lett. **3**, 729 (1987).
[21] D. Ertas and M. Kardar, Phys. Rev. E **49**, R2532 (1994).
[22] R. Golestanian and E. Raphaël, Europhys. Lett. **55**, 228 (2001).
[23] H. Tavana, G. C. Yang, C. M. Yip, D. Appelhans, S. Zschoche, K. Grundke, M. L. Hair, and A. W. Neumann, Langmuir **22**, 628 (2006).
[24] N. Rehse, C. Wang, M. Hund, M. Geoghegan, R. Magerle, and G. Krausch, Eur. Phys. J. E **4**, 69 (2001).
[25] L. Brusch, H. Kühne, U. Thiele, and M. Bär, Phys. Rev. E **66**, 011602 (2002).
[26] U. Thiele, L. Brusch, M. Bestehorn, and M. Bär, Eur. Phys. J. E **11**, 255 (2003).
[27] T. Podgorski, J.-M. Flesselles, and L. Limat, Phys. Rev. Lett. **87**, 036102 (2001).
[28] N. Le Grand, A. Daerr, and L. Limat, J. Fluid Mech. **541**, 293 (2005).
[29] J. B. Brzoska, F. Brochard-Wyart, and F. Rondelez, Langmuir **9**, 2220 (1993).
[30] F. Brochard, Langmuir **5**, 432 (1989).
[31] E. Raphaël, C. R. Acad. Sci. Ser. II **306**, 751 (1988).
[32] M. K. Chaudhury and G. M. Whitesides, Science **256**, 1539 (1992).
[33] S. Daniel, M. K. Chaudhury, and J. C. Chen, Science **291**, 633 (2001).
[34] S. Daniel and M. K. Chaudhury, Langmuir **18**, 3404 (2002).
[35] S. Moulinet, C. Guthmann, and E. Rolley, Eur. Phys. J. B **37**, 127 (2004).
[36] P. Le Doussal, K. J. Wiese, E. Raphaël, and R. Golestanian, Phys. Rev. Lett. **96**, 015702 (2006).
[37] E. Raphaël and P. G. de Gennes, J. Chem. Phys. **90**, 7577 (1989).
[38] J. A. Marsh and A. M. Cazabat, Phys. Rev. Lett. **71**, 2433 (1993).
[39] U. Thiele and E. Knobloch, New J. Phys. **8**, 313 (2006).
[40] U. Thiele and E. Knobloch, Phys. Rev. Lett. **97**, 204501 (2006).
[41] P. Beltrame, P. Hänggi, and U. Thiele, Europhys. Lett. **86**, 24006 (2009).
[42] L. Kondic and J. A. Diez, Phys. Rev. E **65**, 045301 (2002).
[43] L. Kondic and J. Diez, Colloids Surf. A **214**, 1 (2003).
[44] T. Cubaud and A. Fermigier, J. Colloid Interface Sci. **269**, 171 (2004).
[45] X. Y. Zhang and Y. L. Mi, Langmuir **25**, 3212 (2009).
[46] M. Gleiche, L. F. Chi, and H. Fuchs, Nature (London) **403**, 173 (2000).
[47] H. C. Kim, X. Q. Jia, C. M. Stafford, D. H. Kim, T. J. McCarthy, M. Tuominen, C. J. Hawker, and T. P. Russell, Adv. Mater. **13**, 795 (2001).
[48] A. A. Darhuber, J. M. Davis, S. M. Troian, and W. W. Reisner, Phys. Fluids **15**, 1295 (2003).
[49] O. Kuksenok, D. Jasnow, J. Yeomans, and A. C. Balazs, Phys. Rev. Lett. **91**, 108303 (2003).
[50] A. A. Darhuber, J. Z. Chen, J. M. Davis, and S. M. Troian, Philos. Trans. R. Soc. London, Ser. A **362**, 1037 (2004).
[51] S. Lindström and H. Andersson-Svahn, Biochim. Biophys. Acta (2010), doi:10.1016/j.bbagen.2010.04.009.
[52] U. Thiele, e-print arXiv:1010.2920, J. Fluid. Mech. (to be published).
[53] S. H. Strogatz, *Nonlinear Dynamics and Chaos* (Addison-Wesley, Reading, MA, 1994).
[54] P. Beltrame and U. Thiele, SIAM J. Appl. Dyn. Syst. **9**, 484 (2010).
[55] J. A. F. Plateau, *Statique Expérimentale et Théorique des Liquides Soumis aux Seules Forces Moléculaires* (Gauthier-Villars, Paris, 1873).
[56] Lord Rayleigh, Proc. R. Soc. London **29**, 71 (1879).
[57] S. H. Davis, J. Fluid Mech. **98**, 225 (1980).
[58] M. Grinfeld, Mech. Res. Commun. **21**, 613 (1994).
[59] R. H. Weiland and S. H. Davis, J. Fluid Mech. **107**, 261 (1981).
[60] A. Oron, S. H. Davis, and S. G. Bankoff, Rev. Mod. Phys. **69**, 931 (1997).
[61] *Thin Films of Soft Matter*, edited by S. Kalliadasis and U. Thiele (Springer, Vienna, 2007).
[62] G. F. Teletzke, H. T. Davis, and L. E. Scriven, Rev. Phys. Appl. **23**, 989 (1988).
[63] A. Sharma, Langmuir **9**, 861 (1993).
[64] U. Thiele, M. G. Velarde, and K. Neuffer, Phys. Rev. Lett. **87**, 016104 (2001).
[65] U. Thiele, K. Neuffer, Y. Pomeau, and M. G. Velarde, Colloids Surf. A **206**, 135 (2002).
[66] A. Sharma and R. Khanna, Phys. Rev. Lett. **81**, 3463 (1998).
[67] A. Sharma and R. Khanna, J. Chem. Phys. **110**, 4929 (1999).
[68] U. Thiele, M. G. Velarde, K. Neuffer, and Y. Pomeau, Phys. Rev. E **64**, 031602 (2001).
[69] J. Becker, G. Grün, R. Seemann, H. Mantz, K. Jacobs, K. R. Mecke, and R. Blossey, Nat. Mater. **2**, 59 (2003).
[70] U. Thiele, Eur. Phys. J. E **12**, 409 (2003).
[71] E. Doedel, H. B. Keller, and J. P. Kernevez, Int. J. Bifurcation Chaos Appl. Sci. Eng. **1**, 493 (1991).
[72] E. Doedel, H. B. Keller, and J. P. Kernevez, Int. J. Bifurcation Chaos Appl. Sci. Eng. **1**, 745 (1991).
[73] E. J. Doedel, R. C. Paffenroth, A. R. Champneys, T. F. Fairgrieve, Y. A. Kuznetsov, B. E. Oldeman, B. Sandstede, and X. J. Wang, AUTO2000: Continuation and bifurcation software for ordinary differential equations, Concordia University, Montreal, 1997.
[74] A. L. Bertozzi, G. Grün, and T. P. Witelski, Nonlinearity **14**, 1569 (2001).
[75] U. Thiele, K. Neuffer, M. Bestehorn, Y. Pomeau, and M. G. Velarde, Colloids Surf. A **206**, 87 (2002).
[76] J. Becker and G. Grün, J. Phys. Condens. Matter **17**, S291 (2005).
[77] R. A. Friesner, L. S. Tuckerman, B. C. Dornblaser, and T. V. Russo, J. Sci. Comput. **4**, 327 (1989).
[78] B. J. Lowry and P. H. Steen, J. Fluid Mech. **330**, 189 (1997).
[79] Y. J. Chen, N. D. Robinson, J. M. Herndon, and P. H. Steen, Comput. Methods Appl. Mech. Eng. **170**, 209 (1999).
[80] M. Brinkmann, J. Kierfeld, and R. Lipowsky, J. Phys. Condens. Matter **17**, 2349 (2005).
[81] J. R. King, A. Münch, and B. Wagner, Nonlinearity **19**, 2813 (2006).

[82] S. Mechkov, M. Rauscher, and S. Dietrich, Phys. Rev. E **77**, 061605 (2008).
[83] M. Brinkmann and R. Lipowsky, J. Appl. Phys. **92**, 4296 (2002).
[84] P. Hirschberg and E. Knobloch, Nonlinearity **11**, 89 (1998).
[85] U. Thiele and E. Knobloch, Physica D **190**, 213 (2004).
[86] J. H. Siggers, J. Fluid Mech. **475**, 357 (2003).
[87] J. Harlim and W. F. Langford, Int. J. Bifurcation Chaos Appl. Sci. Eng **17**, 2547 (2007).
[88] A. Arneodo, P. H. Coullet, E. A. Spiegel, and C. Tresser, Physica D **14**, 327 (1985).
[89] P. Ashwin, A. M. Rucklidge, and R. Sturman, Physica D **194**, 30 (2004).
[90] B. Krauskopf and B. E. Oldeman, Nonlinearity **17**, 1119 (2004).
[91] G. Dangelmayr, J. Hettel, and E. Knobloch, Nonlinearity **10**, 1093 (1997).
[92] B. Krauskopf and B. E. Oldeman, Nonlinearity **19**, 2149 (2006).
[93] W. F. Langford and K. Zhan, Fields Inst. Commun. **24**, 365 (1999).
[94] H. K. Moffatt, J. de Mécanique **16**, 651 (1977).
[95] F. Melo, Phys. Rev. E **48**, 2704 (1993).
[96] S. T. Thoroddsen and L. Mahadevan, Exp. Fluids **23**, 1 (1997).